NASA Technical Paper 3101

September 1991

Numerical Analysis and Simulation of an Assured Crew Return Vehicle Flow Field

K. James Weilmuenster,
Robert E. Smith, Jr.,
and Francis A. Greene

NASA

NASA Technical Paper 3101

1991

Numerical Analysis and Simulation of an Assured Crew Return Vehicle Flow Field

K. James Weilmuenster,
Robert E. Smith, Jr.,
and Francis A. Greene
Langley Research Center
Hampton, Virginia

National Aeronautics and Space Administration
Office of Management
Scientific and Technical Information Program

Abstract

A lifting body has been proposed as a candidate for the ACRV (assured crew return vehicle), which will serve as the crew rescue vehicle for Space Station *Freedom*. The focus of this work is on body surface definition, surface and volume grid definition, and the computation of inviscid flow fields about the vehicle at wind-tunnel conditions. Very good agreement is shown between the computed aerodynamic characteristics of the vehicle at Mach 10 and those measured in wind-tunnel tests at high Reynolds numbers.

Introduction

Currently within NASA, there is an ongoing activity to define candidate approaches for crew rescue from Space Station *Freedom*. In-house NASA studies have shown that a station-based rescue vehicle will be required for assured crew return if the Space Shuttle is not operational, if there is an emergency that requires abandoning *Freedom*, or if there is a medical emergency that requires evacuation of the crew to Earth. A number of assured crew return vehicle (ACRV) concepts that have been proposed for study over the next 2 years are shown in figure 1. The concepts range from blunt bodies, much like the Apollo shape, to a lifting-body shape derived from work initiated by NASA and the U.S. Air Force in the late sixties when studying the Dynasoar, HL-10, X-24, and M2-F2 vehicles.

As part of the ACRV activity, the Space Systems Division at Langley Research Center has been studying the lifting-body concept. This proposed vehicle, which is currently envisioned to be about 25 ft long, will have the capability to return eight people to Earth from Space Station *Freedom* and land on conventional runways. The lifting-body concept is the most sophisticated of those being studied for the Space Station *Freedom* rescue mission. The complex aerodynamic shape of the vehicle can be seen in figure 1, along with the wings located outboard on the body and the small centerline vertical tail. Wind-tunnel tests indicate that the vehicle will have very good flight characteristics. The purpose of the work reported herein is to establish a computational fluid dynamics (CFD) capability to support system studies and experimental testing of the lifting-body concept. These capabilities would include a determination of inviscid and viscous flow fields at a wind-tunnel condition and a comparison of computed aerodynamic characteristics of the vehicle with those determined through wind-tunnel testing.

Symbols

$\mathbf{A}$	inviscid flux Jacobian matrix
$\mathbf{A}_i, \mathbf{B}_i, \mathbf{C}_i, \mathbf{D}_i$	vectors of cubic-spline coefficients
$\overline{\mathbf{A}}_{I,k}, \overline{\mathbf{B}}_{I,k}, \overline{\mathbf{C}}_{I,k}, \overline{\mathbf{D}}_{I,k}$	vectors of spline coefficients in streamline direction
a, b	inviscid flux volume weighting parameters
$a_{x_i}, b_{x_i}, c_{x_i}, d_{x_i}, a_{y_i}, b_{y_i}, c_{y_i}, d_{y_i}$	cubic-spline coefficients
C	nondimensional speed of sound
C_A	axial-force coefficient
C_m	pitching-moment coefficient
C_N	normal-force coefficient
$\frac{Dt}{D\xi}(\xi_e)$	derivative at inflection point
$\mathbf{D}$	summation of flux differences
$\frac{d\mathbf{X}_i}{dt}$	vector of first spline derivative
$\frac{d^2\mathbf{X}_i}{dt^2}$	vector of second spline derivative
E	nondimensional total energy per unit volume
E'	dimensional total energy per unit volume, kg/m-sec^2
$\mathbf{E}, \mathbf{F}, \mathbf{G}$	flux vectors in ξ, η, and ζ directions
e	nondimensional internal energy per unit mass
e'	dimensional internal energy per unit mass, m^2/sec^2
$\mathbf{H}$	flux vector normal to cell face
$\mathbf{h}$	Cartesian flux vector
I	index for grid points in circumferential direction
i, j, k	indices of cell centers in ξ, η, and ζ directions, respectively, or index of measured points
K	number of grid points in streamwise direction
L	normalizing reference length, m
L/D	lift-drag ratio
M	number of grid points in streamwise direction

M_∞	free-stream Mach number
$\mathbf{M}$	right inviscid Jacobian eigenvector matrix
$\mathbf{M}^{-1}$	left inviscid Jacobian eigenvector matrix
m	number of measured sections in streamwise direction
N	number of grid points around vehicle
n	current time level
n_k	number of measured points on kth section
$\mathbf{n}$	unit vector normal to cell face
P	nondimensional pressure
P'	dimensional pressure, N/m^2
p	dummy index for i, j, or k
$\mathbf{q}$	dependent variable vector
R	Reynolds number
S'	velocity, m/sec
$\overline{S}_I$	set of spline coefficients in streamwise direction
S_k	set of all spline coefficients for kth section
s	streamwise parametric variable
t	time, sec, or parametric independent variable
$\bar{t}$	intermediate parametric variable
t_e	parametric variable value at inflection point
t_i	ith value of parametric variable
t_n	last value of parametric variable
$\mathbf{U}$	nondimensional velocity in direction normal to cell face
u, v, w	nondimensional Cartesian velocity components in x, y, and z directions
u', v', w'	dimensional Cartesian velocity components in x, y, and z directions, m/sec
$\mathbf{V}$, $\mathbf{W}$	nondimensional velocities in direction tangent to cell face
$\mathbf{X}$	vector of coordinate functions
$\mathbf{X}_m(t_i)$	vector of measured coordinates
$\mathbf{X}''(t)$	vector of second derivatives
x, y, z	nondimensional Cartesian coordinates
$x(t), y(t)$	coordinates as a function of parametric variable
$\bar{x}, \bar{y}, \bar{z}$	interpolated coordinates for streamwise smoothing
x', y', z'	dimensional Cartesian coordinates, m
x_i, y_i	ith cross-sectional coordinates
α	angle of attack, deg
Γ_1, Γ_2	grid concentration parameters
Γ_3	concentration control parameter for streamwise direction
γ	ratio of specific heats
$\Delta(\ )$	spatial change in quantity, $(\ )_R - (\ )_L$
$\delta(\ )$	time change in quantity, $(\ )^{n+1} - (\ )^n$
$\delta\mathbf{X}_i$	vector of allowable deviations
ϵ	positive constant
ζ	computational coordinate in streamwise direction
η	computational coordinate
$\boldsymbol{\lambda}$	inviscid Jacobian eigenvalue matrix
ξ	computational coordinate around configuration
ξ_e	computational coordinate inflection value
ρ	nondimensional density
ρ'	dimensional density, kg/m^3
$\boldsymbol{\sigma}$	nondimensional cell-face area
Ω	nondimensional cell volume

Subscripts:

L	quantity at cell center to left of cell face

R	quantity at cell center to right of cell face
∞	free-stream value
Superscripts:	
n	time level
T	transpose
$+$	quantity associated with positive eigenvalue
$-$	quantity associated with negative eigenvalue
$*$	latest available data
$'$	dimensional quantities

Geometry

All computational fluid dynamics simulations require the generation of a grid that covers the flowfield domain and its boundaries. To obtain an accurate solution, the grid must be concentrated in regions with large gradients, and the grid must possess favorable mathematical characteristics, such as acceptable grid skewness.

For the flow about an aerospace vehicle such as the ACRV, a grid on the configuration boundary surface must be created and integrated into an overall grid. The vehicle surface grid is extracted from a numerical model obtained from either a computer-aided design (CAD) system or from measurement of a physical model.

The numerical model of the ACRV vehicle was obtained from the measurement of a 5.9-in-long wind-tunnel model. The measuring instrument obtains two coordinates around the model at fixed stations in the third coordinate. When the vehicle geometry is defined in a right-hand Cartesian coordinate system (fig. 2), the origin of the coordinate system is at the most forward point of the vehicle. The negative z-axis extends down the vehicle, the y-axis is in the spanwise direction, and the x-axis is in the vertical direction. The measured data base consists of x and y surface coordinates at 20 z-coordinate stations (cross sections) down the vehicle. (See fig. 3.)

Measured coordinates have associated measurement errors, and there is the possibility of roughness on the model itself, which occurs in the manufacturing process. An inspection of the plotted cross sections of the ACRV model revealed, from a computational standpoint, a number of serious irregularities that could be the result of measurement error or surface roughness. These irregularities are illustrated in figure 4, which shows a plot of the original measured surface points at the 15th station along the body. The solid line represents a spline fit of the measured data points. Inspection of this plot does not reveal any noticeable surface imperfections. However, the expanded views of three surface sections enclosed by the boxes labeled 1, 2, and 3 and shown in figures 4(b), 4(c), and 4(d), respectively, show surface irregularities present in the measured data. If the irregularities are allowed in the computational grid, they will also appear in the numerical solution. Alternatively, the numerical model can be initially idealized by smoothing the measured surface coordinates. There may also be surface characteristics that are not to be included in a CFD solution. For instance, the vertical stabilizer is not included in the initial computations.

Surface Smoothing

To remove imperfections in the measured data, a cubic-spline smoothing algorithm (ref. 1) is applied to the coordinates at each z-coordinate cross section. The application of the algorithm starts with the creation of a parametric independent variable t, which is the approximated arc length along a cross section. The x and y coordinates are considered to be functions $x(t)$ and $y(t)$. The functions are determined from the sets of parametric data

$$\{x_i, t_i\}_{i=1}^{i=n} \qquad \text{and} \qquad \{y_i, t_i\}_{i=1}^{i=n}$$

where x_i and y_i are ith measured coordinates on a cross section, t_i is the approximate arc length at the ith point, and n is the number of measured points on a cross section; n varies from cross section to cross section. The approximate arc length is defined by

$$t_{i+1} = \left[(x_{i+1} - x_i)^2 + (y_{i+1} - y_i)^2\right]^{1/2} + t_i$$

where $t_1 = 0$. This computation starts on the bottom of the vehicle at the symmetry plane and continues around to the top of the vehicle at the symmetry plane. After the maximum approximate arc length is computed, the variable t is redefined to be the normalized approximate arc length by

$$t_i = \frac{t_i}{t_n}$$

The functions $x(t)$ and $y(t)$ are represented in vector form

$$\mathbf{X}(t) = \begin{bmatrix} x(t) \\ y(t) \end{bmatrix}$$

and the cubic-spline representation is

$$\mathbf{X}(t) = \Big[\mathbf{A}_i + \mathbf{B}_i(t-t_i) + \mathbf{C}_i(t-t_i)^2 + \mathbf{D}_i(t-t_i)^3\Big]_{i=1}^{i=n-1} \quad (1)$$

where

$$\mathbf{A}_i = \begin{bmatrix} a_{x_i} \\ a_{y_i} \end{bmatrix} \qquad \mathbf{B}_i = \begin{bmatrix} b_{x_i} \\ b_{y_i} \end{bmatrix}$$

$$\mathbf{C}_i = \begin{bmatrix} c_{x_i} \\ c_{y_i} \end{bmatrix} \qquad \mathbf{D}_i = \begin{bmatrix} d_{x_i} \\ d_{y_i} \end{bmatrix}$$

The spline conditions are

$$(\mathbf{X}_i)_{t_{i+1}} = (\mathbf{X}_{i+1})_{t_{i+1}}$$

$$\left(\frac{d\mathbf{X}_i}{dt}\right)_{t_{i+1}} = \left(\frac{d\mathbf{X}_{i+1}}{dt}\right)_{t_{i+1}}$$

$$\left(\frac{d^2\mathbf{X}_i}{dt^2}\right)_{t_{i+1}} = \left(\frac{d^2\mathbf{X}_{i+1}}{dt}\right)_{t_{i+1}}$$

where

$$i = 1,\ 2,\ \cdots,\ n-2$$

and where $0 < t < t_n$. The coefficients

$$\{\mathbf{A}_i, \mathbf{B}_i, \mathbf{C}_i, \mathbf{D}_i\}_{i=1}^{i=n-1}$$

are undetermined parameters whose values define $\mathbf{X}(t)$ in equation (1). The objective is to find the coefficients that minimize the integral of the second derivatives squared as follows:

$$\int_0^{t_n} [\mathbf{X}''(t)]^2\, dt$$

subject to the constraint

$$\sum_{i=1}^{n} \frac{[\mathbf{X}(t_i) - \mathbf{X}_m(t_i)]^2}{\delta\mathbf{X}_i} \le \epsilon \quad (2)$$

where

$$\mathbf{X}_m(t_i) = \begin{bmatrix} x_i \\ y_i \end{bmatrix}$$

$$\delta\mathbf{X}_i = \begin{bmatrix} \delta x_i \\ \delta y_i \end{bmatrix}$$

and E is a positive constant that specifies the extent of smoothing. The vector $\delta\mathbf{X}$ is the allowable deviation of the spline function $\mathbf{X}(t)$ and the measured surface coordinates $\mathbf{X}_m$. The restated objective is to find the smoothest cubic spline that passes within the following bounds:

$$\mathbf{X}_m(t_i) - \delta\mathbf{X}_i \le \mathbf{X}_m(t_i) \le \mathbf{X}_i(t_m) + \delta\mathbf{X}_i$$

where $\delta\mathbf{X}_i$ is the maximum deviation of the spline functions from the measured coordinates. The method of Lagrange multipliers from the calculus of variations is used to find the parameters

$$\mathbf{S}_k = \{\mathbf{A}_i, \mathbf{B}_i, \mathbf{C}_i, \mathbf{D}_i\}_{i=1}^{i=n_k}$$

where k is the kth cross section in the streamwise direction. The solution algorithm for spline smoothing can be found in reference 1. The technique exists in subroutine form (SUBROUTINE CSDSES) in the Langley math library. (See ref. 2.) A main program is written to read the measured coordinates, compute the approximate arc length, and call the spline-smoothing subroutine for each coordinate. It is necessary to provide the allowable deviations, $\{\delta\mathbf{X}_i\}_{i=1}^{i=n_k}$, and the one constant ϵ, which is an estimate of the sum of the normalized deviations squared in equation (2), is set equal to $n_k - 1$. Figures 5 and 6 show the application of the smoothing procedure to two cross sections from the ACRV vehicle (one near the front of the vehicle and one near the rear of the vehicle). Figures 5(a) and (b) and figures 6(a) and (b) show the y versus t and x versus t smoothing; figures 5(c) and 6(c) show the x versus y cross section. The algorithm is applied to each measured cross section.

Surface Grid

The technique described previously smoothes the measured data at each cross section in only one direction. The next step is to distribute points along the smoothed cross sections in a fashion that is desired for the final grid points. These points are then smoothed and interpolated in the streamwise direction for the surface grid points. The initial desired circumferential distribution of points on the ACRV vehicle is uniform around the vehicle near the front and concentrated at the wingtip as the wing emerges from the fuselage downstream. The streamwise distribution should be concentrated near the front of the vehicle.

If N is the number of grid points around the body, and the index I denotes the ith grid point, a computational coordinate ξ around the body is defined by

$$\xi = \frac{(I-1)}{(N-1)}$$

and ξ is mapped into the normalized approximate arc length t with the variable $\bar{t}$. Interpolated $\bar{x}$ and $\bar{y}$ coordinates are obtained from S_k and equation (1) given $\bar{t}$. In the streamline direction and up to the wing root, the desired grid spacing is uniform and $\bar{t} = \xi$. At the wing root, the distribution becomes a bi-exponential that is defined by

$$\bar{t} = t_e \frac{\exp(\Gamma_1 \xi) - 1}{\exp(\Gamma_1) - 1} \qquad (0 \le \xi \le \xi_e;\ 0 \le \bar{t} \le t_e)$$

and

$$\bar{t} = t_e + (1 - t_e) \frac{\exp\left(\Gamma_2 \frac{\xi - \xi_e}{1 - \xi_e}\right) - 1}{\exp(\Gamma_2) - 1} \qquad (\xi_e \le \xi \le 1;\ \bar{t}_e \le t \le 1)$$

The symbol ξ_e is the desired percentage of grid points around the bottom of the vehicle up to the wing leading edge, and t_e is the normalized approximate arc length along the same curve up to the wing leading edge. The constant Γ_1 governs the amount of concentration at the wingtip, and Γ_2 is computed by using a Newton-Raphson iteration to assure continuity of $(Dt/D\xi)\xi_e$. The parameters ξ_e, t_e, and Γ_1 vary in the streamwise direction from the wing root to the end of the wing. The computation of the surface grid is based on smoothing the previously defined data in the streamwise direction. The parametric form of the smoothed cross-sectional data is

$$\{\bar{x}_{I,k}, s_{I,k}\}_{I=1,k=1}^{I=N,k=m}$$

$$\{\bar{y}_{I,k}, s_{I,k}\}_{I=1,k=1}^{I=N,k=m}$$

$$\{\bar{z}_k, s_{I,k}\}_{k=1}^{k=m}$$

where $\bar{z}_k$ is the negative z coordinate of the kth cross section, m is the number of cross sections, and s is the normalized approximate arc length in the streamwise direction defined by

$$s_{I,k+1} = \left[(\bar{x}_{I,k+1} - \bar{x}_{I,k})^2 + (\bar{y}_{I,k+1} - \bar{y}_{I,k})^2 + (\bar{z}_{k+1} - \bar{z}_k)^2\right]^{1/2} + s_{I,k}$$

$$s_{I,1} = 0$$

The computation of $s_{I,k}$ starts at the nose of the vehicle and ends at $k = m$. Again, after the maximum approximate arc length is computed for each value of I, s is normalized with respect to the maximum value. The same procedure that was used to represent a cubic-spline approximation for $\mathbf{X}(t)$ is used to compute $\mathbf{X}(I, s)$ where

$$\mathbf{X}(I, s) = \begin{bmatrix} \bar{x}(I, s) \\ \bar{y}(I, s) \\ \bar{z}(I, s) \end{bmatrix}$$

and the cubic-spline representation is

$$\mathbf{X}(I, s) = \Big[\overline{\mathbf{A}}_{I,k} + \overline{\mathbf{B}}_{I,k}(s - s_{I,k}) + \overline{\mathbf{C}}_{I,k}(s - s_{I,k})^2 + \overline{\mathbf{D}}_{I,k}(s - s_{I,k})^3\Big]_{I=1,k=1}^{I=N,k=m} \qquad (3)$$

where

$$\overline{\mathbf{A}}_{I,k} = \begin{bmatrix} a_{x_{I,k}} \\ a_{y_{I,k}} \\ a_{z_{I,k}} \end{bmatrix} \qquad \overline{\mathbf{B}}_{I,k} = \begin{bmatrix} b_{x_{I,k}} \\ b_{y_{I,k}} \\ b_{z_{I,k}} \end{bmatrix}$$

$$\overline{\mathbf{C}}_{I,k} = \begin{bmatrix} c_{x_{I,k}} \\ a_{y_{I,k}} \\ a_{z_{I,k}} \end{bmatrix} \qquad \overline{\mathbf{D}}_{I,k} = \begin{bmatrix} d_{x_{I,k}} \\ d_{y_{I,k}} \\ b_{z_{I,k}} \end{bmatrix}$$

The procedure described above is used to compute

$$\overline{\mathbf{S}}_I = \left[\overline{\mathbf{A}}_{I,k}, \overline{\mathbf{B}}_{I,k}, \overline{\mathbf{C}}_{I,k}, \overline{\mathbf{D}}_{I,k}\right]_{I=1,k=1}^{I=N,k=M}$$

where

$$\delta\mathbf{X}_{I,k} = \begin{bmatrix} \delta_{\bar{x}_{I,k}} \\ \delta_{\bar{y}_{I,k}} \\ \delta_{\bar{z}_{I,k}} \end{bmatrix}$$

If M is the total number of grid points along the body in the streamwise direction, and if the index k is the kth grid point, a computational coordinate ζ along the vehicle is defined by

$$\zeta = \frac{k - 1}{M - 1}$$

and ζ is mapped into the normalized approximate arc length s. A concentration of grid points near the front of the vehicle is achieved by using the transformation

$$\bar{s} = \frac{\exp(\Gamma_3 \zeta) - 1}{\exp(\Gamma_3) - 1}$$

The constant Γ_3 determines the amount of concentration. A surface grid

$$[x(I,K), y(I,K), z(I,K)]_{I=1,K=1}^{I=N,K=M}$$

is obtained by evaluating equation (3) and with a given value of s.

Starting with the measured data, a surface grid for the ACRV vehicle where $N = 81$ and $M = 125$ is shown in figure 7. This boundary surface grid is then used in the computation of the volume grid about the vehicle on which Euler flow is simulated.

Volume Grid

The initial flow-field computations about the ACRV are obtained at a high Mach number and a high angle of attack. Under these conditions, the bow shock lies close to the body on the windward side and far from the body on the leeward side. The need for the volume grid to extend beyond the outer limits of this shock dictates the structure of the volume grid.

The grid topology chosen for the ACRV flow field is a dual-block topology similar to that described in reference 3. In this topology, there is an inner block that begins from a singularity line just upstream of the wing root. A second block surrounds the forward part of the vehicle and the inner block. The general representation of the two-block topology is shown in figure 8. In reference 3, the lifting surfaces on the configurations have sharp leading edges, whereas the ACRV wing has a rounded leading edge. Consequently, the outer-boundary surface of the inner-grid block is displaced forward of the wing leading edge so that a C-type grid is formed spanwise about the wing.

The advantage of a two-block topology over a one-block topology is that the flow-field region can be adequately covered with fewer points. That is, to have enough points to cover the region between the wing and symmetry plane, a single block would require many more points in the forward region than is necessary. The disadvantages are the additional program complexity in the solution code and the numerical complications at the singularity line.

Inner-Block Volume Grid

The inner block is bounded by the vehicle surface, the outer-boundary surface of the inner block, the bottom-symmetry surface, the top-symmetry surface, the singularity line, and the downstream surface (fig. 9). The outer-boundary surface is defined by creating an analytical curve, translating the curve to the singularity line, and rotating it around the vehicle. It is then stretched in the spanwise direction and skewed upward as it passess over the top of the vehicle. This process is similar to the surface boundary generation that is described in reference 3, with the addition of the stretching and skewing. The interior grid and the distribution of grid points on the outer-boundary surface, the symmetry-plane surfaces, and the downstream surface are computed by using a three-dimensional version of the two-boundary grid generation (TBGG) technique described in reference 4. The grid points are concentrated at the vehicle surface, and near orthogonality is maintained. Figure 10 shows the inner grid on the downstream boundary surface. As the line of singularity is approached from downstream, the distribution becomes more uniform and matches the distribution upstream of the singularity line.

Outer-Block Volume Grid

The grid on the outer block surrounds the forward part of the fuselage and the grid on the inner block. The six surfaces that form the outer block are (1) the forward fuselage and outer-boundary surface on the inner block, (2) a far-field boundary surface, (3) the symmetry plane on the bottom side of the vehicle, (4) the symmetry plane on the top side of the vehicle, (5) a polar singularity line from the (0,0,0) point of the vehicle to the far-field boundary surface, and (6) a downstream surface that extends the inner block to the far-field boundary.

The first computation for the outer block is the far-field boundary surface, which is similar to computing the outer-boundary surface for the inner-grid block. The characteristics of the far-field boundary are that it is relatively close to the vehicle on the bottom side and relatively far away on the top side to be just outside of the bow shock. Also, it should expand away from the wings in the spanwise direction to capture the shock phenomenon.

Instead of using a single analytical curve and rotating it around the vehicle, two curves are blended in the streamwise direction to create another curve that is translated to a point about four shock standoff distances from the nose and rotated about the vehicle while being stretched in the spanwise and vertical directions. The two blended curves are chosen such that one is suitable forward and the other is suitable rearward. Grid points are distributed rearward and around the outer boundary to be approximately across from the corresponding points on the surface of the opposite side. A side view of the far-field surface is shown in figure 11.

The general approach for computing the outer-block grid is transfinite interpolation (ref. 5), given grid point information at block boundaries and intermediate surfaces. The outer-block computation is divided into two parts: (1) the forward part from the nose singularity line back to a surface extending from the singularity line around the fuselage to the far-field boundary (singularity-line surface), and (2) the rearward part extending from the singularity-line surface to the downstream surface.

The forward part of the outer block is obtained by first computing grid points on the bottom symmetry plane, on the top symmetry plane, and on a spanwise surface nearly orthogonal to the symmetry plane. The TBGG algorithm is applied to concentrate grid points near the vehicle surface and maintain near orthogonality. Figure 12 shows the three surfaces. Transfinite interpolation with linear-exponential blending functions is used to fill in the interior. The rearward part on the outer block is computed by using transfinite interpolation with Lagrangian blending functions. (See ref. 6.) This method allows first-derivative continuity in grid spacing and grid-curve direction except in the vicinity of the singularity line. A concentration of grid points in this region is used to overcome this deficiency. Figure 13 shows grid points in the symmetry plane and two spanwise surfaces in the streamwise direction.

Solution Technique

The solution technique is based on the Langley Aerothermodynamic Upwind Relaxation Algorithm (LAURA) code discussed in reference 7; LAURA is a viscous code that has been modified to compute inviscid flow fields. A brief description of the LAURA code, which is an upwind finite-volume algorithm, and the implementation of the inviscid boundary condition are given in this section.

Governing Equations

The integral form of the governing equations can be expressed as

$$\iiint \mathbf{q}_t \, d\Omega + \iint \mathbf{h} \cdot \mathbf{n} \, d\boldsymbol{\sigma} = 0 \tag{4}$$

where $\mathbf{q}_t$ is the time rate of change of the dependent variable vector at a cell center, $\mathbf{h}$ is the Cartesian flux vector, and $\mathbf{n}$ is the outward unit normal vector to a cell face. The cell volume and cell-face area are represented by Ω and $\boldsymbol{\sigma}$, respectively. The quantity $\mathbf{h} \cdot \mathbf{n}$ is the flux vector normal to a cell face. The vector $\mathbf{h}$ can be written in terms of its components in the x, y, and z directions as

$$\mathbf{h} = \mathbf{E}_x + \mathbf{F}_y + \mathbf{G}_z \tag{5}$$

where

$$\mathbf{q} = [\rho, \rho u, \rho v, \rho w, E]^T \tag{6}$$

$$\mathbf{E} = [\rho u, \rho u^2 + P, \rho uv, \rho uw, (E + P)u]^T \tag{7}$$

$$\mathbf{F} = [\rho v, \rho uv, \rho v^2 + P, \rho vw, (E + P)v]^T \tag{8}$$

$$\mathbf{G} = [\rho w, \rho uw, \rho vw, \rho w^2 + P, (E + P)w]^T \tag{9}$$

All quantities have been nondimensionalized as shown in the following equations:

$$\rho = \frac{\rho'}{\rho'_\infty} \quad u = \frac{u'}{S'_\infty} \quad v = \frac{v'}{S'_\infty} \quad w = \frac{w'}{S'_\infty}$$

$$P = \frac{P'}{\rho'_\infty (S'_\infty)^2} \quad e = \frac{e'}{(S'_\infty)^2} \quad E = \frac{E'}{\rho'_\infty (S'_\infty)^2}$$

$$x = \frac{x'}{L'} \quad y = \frac{y'}{L'} \quad z = \frac{z'}{L'}$$

The value L' is a user-defined reference length. The equation set is closed by using the ideal gas law.

Expressing equation (4) in finite-volume form for a single six-sided cell in the computational domain gives

$$\delta \mathbf{q}_{i,j,k} = \left(\frac{\delta t}{\Omega}\right)_{i,j,k} \Big(\mathbf{H}^*_{i-1/2,j,k}\ \boldsymbol{\sigma}_{i-1/2,j,k} - \mathbf{H}^*_{i+1/2,j,k}\ \boldsymbol{\sigma}_{i+1/2,j,k} + \mathbf{H}^*_{i,j-1/2,k}\ \boldsymbol{\sigma}_{i,j-1/2,k} - \mathbf{H}^*_{i,j+1/2,k}\ \boldsymbol{\sigma}_{i,j+1/2,k} + \mathbf{H}^*_{i,j,k-1/2}\ \boldsymbol{\sigma}_{i,j,k+1/2} - \mathbf{H}_{i,j,k+1/2}\ \boldsymbol{\sigma}_{i,j,k+1/2} \Big) \tag{10}$$

A shorthand index notation enables equation (10) to be expressed as

$$\delta \mathbf{q}_{i,j,k} = \left(\frac{\delta t}{\Omega}\right)_{i,j,k} \sum_{p=i,j,k} \left[(\mathbf{H}^* \boldsymbol{\sigma})_{p-1/2} - (\mathbf{H}^* \boldsymbol{\sigma})_{p+1/2} \right] \tag{11}$$

where $\delta \mathbf{q}$ is the change in $\mathbf{q}$ per time step, $\mathbf{H}$ is the inviscid flux normal to a cell face, and δt is the time step. The lowercase subscripts in equations (10) and (11) represent cell-centered values, unless offset by one half, in which case they represent values at the center of a cell face. A diagram of the indexing is shown in figure 14. The equations used to compute the cell volume, the cell-face area, the time step, and the metrics are found in reference 7.

Because the flux normal to a cell face is a function of information on either side of the face (left or right), $\mathbf{H}$ in equations (10) and (11) is expressed as

$$\mathbf{H}^*(\mathbf{q}_L, \mathbf{q}_R) = \frac{1}{2}\left[a\mathbf{H}^*(\mathbf{q}_L) + b\mathbf{H}^*(\mathbf{q}_R)\right] - \frac{1}{2}\mathbf{D}^*(\mathbf{q}_L, \mathbf{q}_R) \tag{12}$$

where L and R denote the indices of the cell centers to the left and right, respectively, of the face being evaluated. The functions a and b are flux weighting parameters defined in terms of cell volumes as

$$a = \frac{2\Omega_R}{\Omega_R + \Omega_L} \qquad b = \frac{2\Omega_L}{\Omega_R + \Omega_L}$$

The parameters a and b lessen the effects of grid stretching, and their formulation is empirical. (See ref. 8.) The variable $\mathbf{D}^*$ in equation (12) is a summation of flux differences. The value $\mathbf{D}^*$ can be determined from the solution of a Riemann initial-value problem. Several solution procedures for $\mathbf{D}^*$ have been developed. The approach adopted in this work is attributed to Roe (ref. 9).

The first-order upwind-biased flux is computed by using the Roe flux-difference splitting (ref. 9). For the first-order flux, the flux difference across the cell face comes from the solution of a Riemann initial-value problem posed by Roe. The initial data for the problem are found at the two cell centers to which the face is common. The flux difference is split into two parts, one associated with the positive and one with the negative eigenvalues of the unsteady inviscid Jacobian matrix. The speed and direction of information propagating toward a cell face are directly proportional to the absolute magnitude of the eigenvalues and sign of the eigenvalues, respectively. That is, negative eigenvalues send information from the right toward a cell face, whereas positive eigenvalues send information from the left; how quickly this information travels is related to the absolute magnitude of the eigenvalue. Roe's method correctly interprets this wave motion relative to a cell face and computes an inviscid flux that correctly models the physics of the flow. The inviscid flux for a supersonic flow with all positive eigenvalues is made up solely of information from the left, and a supersonic flow with all negative eigenvalues is made up solely of information from the right. If the flow has eigenvalues with mixed signs, the inviscid flux is comprised of information from the right and left.

Roe's method gives $\mathbf{D}$ as the exact solution to the following approximate Riemann problem:

$$\mathbf{q}_t + \mathbf{A}\mathbf{q}_x = 0 \tag{13}$$

The change in flux across a cell face for this problem can be expressed as

$$\mathbf{D}(\mathbf{q}_L, \mathbf{q}_R) = \Delta\mathbf{H}_I = \mathbf{H}_I(\mathbf{q}_R) - \mathbf{H}_I(\mathbf{q}_L) = \mathbf{M}\boldsymbol{\lambda}\mathbf{M}^{-1}(\mathbf{q}_L, \mathbf{q}_R)(\mathbf{q}_R - \mathbf{q}_L) \tag{14}$$

where the flux vector Jacobian $\mathbf{A}$ is expressed in terms of its right ($\mathbf{M}$) and left ($\mathbf{M}^{-1}$) eigenvectors and a diagonal matrix of its eigenvalues ($\boldsymbol{\lambda}$). The matrices $\mathbf{A}$, $\boldsymbol{\lambda}$, $\mathbf{M}$, and $\mathbf{M}^{-1}$ are given in reference 7. Representing the positive and negative contributions of the eigenvalues as shown below

$$\boldsymbol{\lambda}^+ = \frac{\boldsymbol{\lambda} + |\boldsymbol{\lambda}|}{2} \qquad \boldsymbol{\lambda}^- = \frac{\boldsymbol{\lambda} - |\boldsymbol{\lambda}|}{2} \tag{15}$$

enables $\mathbf{D}(\mathbf{q}_L, \mathbf{q}_R)$ to be written as

$$\mathbf{D}(\mathbf{q}_L, \mathbf{q}_R) = (\mathbf{M}\boldsymbol{\lambda}^+\mathbf{M}^{-1} - \mathbf{M}\boldsymbol{\lambda}^-\mathbf{M}^{-1})(\mathbf{q}_R - \mathbf{q}_L) \tag{16}$$

or

$$\mathbf{D}^*(\mathbf{q}_L, \mathbf{q}_R) = \mathbf{M}|\boldsymbol{\lambda}|\mathbf{M}^{-1}\Delta\mathbf{q}^* = |\mathbf{A}|\Delta\mathbf{q}^* \tag{17}$$

When equation (16) is substituted into equation (12), the first-order inviscid flux normal to a cell face is

$$\mathbf{H}_I^*(\mathbf{q}_L, \mathbf{q}_R) = \frac{1}{2}\left[a\mathbf{H}_I^*(\mathbf{q}_L) + b\mathbf{H}_I^*(\mathbf{q}_R) - |\mathbf{A}|(\mathbf{q}_R, \mathbf{q}_L)\Delta\mathbf{q}^*\right] \tag{18}$$

The inviscid flux shown in equation (18) can be thought of as being composed of a second-order approximation to the inviscid flux at a cell face (first two terms) minus a dissipation term (remaining term). If this dissipation is not included, the algorithm is equivalent to a centrally differenced algorithm.

For second-order-accurate solutions obtained by using Yee's STVD approach (ref. 10), $\mathbf{D}^*$ in equation (12) can be shown as

$$\mathbf{D}^*(\mathbf{q}_L, \mathbf{q}_R) = \mathbf{M}_2|\boldsymbol{\lambda}|_2\left[\mathbf{M}_2^{-1}\Delta\mathbf{q}_2^* - \text{minmod}\ (\mathbf{M}_1^{-1}\Delta\mathbf{q}_1, \mathbf{M}_2^{-1}\Delta\mathbf{q}_2, \mathbf{M}_3^{-1}\Delta\mathbf{q}_3)\right] \tag{19}$$

The subscript 2 references the face at which the flux is being computed—1, the face behind, and 3, the face ahead. The minmod function compares differences in characteristic variables at these locations and chooses the smallest in absolute magnitude if the signs of the values are the same, or zero if the signs are different. The first term in equation (19) is the first-order term from equation (17), and the second is a correction that makes $\mathbf{D}^*$ second-order accurate if the signs of the differences in characteristic variables being evaluated in the minmod function are the same.

If variables with the superscript * contain information referenced to the i, j, k cell center, they are linearized by the following equation:

$$\mathbf{K}^* = \mathbf{K}^n + \left(\frac{\partial\mathbf{K}^n}{\partial\mathbf{q}}\right)_{i,j,k}\delta\mathbf{q}_{i,j,k}$$

The variable $\mathbf{K}$ is a dummy variable which represents the value being linearized.

Upon substituting equation (12) into equation (11) and performing the requisite linearizations, the governing equations can be written as

$$\left\{I + \left(\frac{\delta t}{2\Omega}\right)_{i,j,k} \sum_{p=i,j,k} \left[(|\mathbf{A}|\boldsymbol{\sigma})_{p+1/2} + (|\mathbf{A}|\sigma)\right]_{p-1/2}\right\}\delta q_{i,j,k}$$

$$= \left(\frac{\delta t}{2\Omega}\right)_{i,j,k} \sum_{p=i,j,k} \left(\{[a\mathbf{H}_I^n(\mathbf{q}_L) + b\mathbf{H}_I^n(\mathbf{q}_R) - \mathbf{D}^n(\mathbf{q}_L, \mathbf{q}_R)]\}\,\sigma_{p-1/2}\right.$$

$$\left. - \{[a\mathbf{H}_I^n(\mathbf{q}_L) + b\mathbf{H}_I^n(\mathbf{q}_R) - \mathbf{D}^n(\mathbf{q}_L, \mathbf{q}_R)]\}\,\sigma_{p+1/2}\right) \tag{20}$$

Boundary Conditions

This algorithm requires that dependent variables be specified both on the surface and at "pseudo" cells located one-half cell below the vehicle surface. In figure 14, (a) denotes the plane of cell-centered values one-half cell above the body surface, (b) denotes the plane of cell-centered values one-half cell below the body surface, and the X denotes the location of points on the surface. The values at (b) are required for the computation of the first- and second-order fluxes associated with the methods of Roe and Yee, respectively. The values used at (b) were based on the values at (a). The Cartesian velocity components at (b) were computed such that the following conditions were satisfied:

$$\mathbf{U}_b = -\mathbf{U}_a$$
$$\mathbf{V}_b = \mathbf{V}_a$$
$$\mathbf{W}_b = \mathbf{W}_a$$

where $\mathbf{U}$ is the contravariant velocity in a direction normal to the body surface, and $\mathbf{V}$ and $\mathbf{W}$ are contravariant velocities in a plane tangent to the body surface. First-order extrapolation was used to compute the internal energy at (b), and the density at (b) was computed by using

$$\left[\frac{(\gamma-1)\rho e}{\rho^\gamma}\right]_a = \left[\frac{(\gamma-1)\rho e}{\rho^\gamma}\right]_b$$

Values on the wall were determined such that surface tangency is enforced. (See ref. 11.) In the method outlined in reference 11, extrapolation is used to determine initial wall values, and a wave correction is then performed on these extrapolated quantities to determine final wall values and to satisfy tangency. In general, just extrapolating values to the surface will not satisfy tangency. The wave correction is shown below, where c represents the wave corrected values and a represents the extrapolated values:

$$\frac{P_a}{\rho_a^\gamma} = \frac{P_c}{\rho_c^\gamma}$$

$$|\mathbf{U}_a| - 2\left(\frac{C_a}{\gamma-1}\right) = |\mathbf{U}_c| - 2\left(\frac{C_c}{\gamma-1}\right)$$

$$\mathbf{U}_c = 0$$
$$\mathbf{V}_a = \mathbf{V}_c$$
$$\mathbf{W}_a = \mathbf{W}_c$$

At the remaining boundaries, *pseudo* cells were also employed. For the outflow boundary, a supersonic outflow boundary condition was used; along the axis singularity and symmetry planes, a reflective boundary condition is used.

Flow-Field Computations and Analysis

Preliminary trajectory analysis indicates that the ACRV vehicle will fly at approximately 25° angle of attack during the hypersonic portion of its flight. Also, a considerable amount of aerodynamic testing will be done in the Langley 31-Inch Mach 10 Tunnel. (See ref. 12.) Therefore, $M_\infty = 10$ and $\alpha = 25°$ have been chosen as the nominal conditions for the following flow-field solution. Also, solutions have been obtained at angles of attack of 15°, 20°, 30°, and 35° to cover the range of available experimental data. Previous analyses (refs. 13 and 14) have shown that a perfect-gas analysis is appropriate when comparing computations with data from this tunnel. Therefore, the ratio of specific heats, γ, was taken to be 1.4 for these computations.

These computations were made on the CRAY-2 computer at Ames Research Center's Numerical Aerodynamic Simulation (NAS) system and on the

CRAY-2 computer at Langley Research Center with the body and grid defined in this paper. This grid of 584 496 points translates into a code requirement of approximately 40 megawords of memory. A complete flow-field solution required about 10 hr of CPU time on the NAS CRAY-2 and about 8 hr of CPU time on the Langley CRAY-2, which is approximately 1.2 times faster than the NAS machine.

Figure 15 shows a pressure contour plot in the symmetry plane for the nominal condition. The extent of the bow shock and the location of the canopy shock can be seen. The apparent smearing of the bow shock approximately half way down the body, and most evident in the windward-symmetry plane, is the result of the shock leaving the "outer" grid, which is closely aligned with the shock, and entering the "inner" grid, which is highly skewed relative to the shock. Nondimensional surface pressures in the symmetry plane are shown in figure 16. The windward-side pressure distribution is typical for this shuttle-like surface. On the leeward side, the flow expands rapidly around the nose, compresses when it encounters the canopy, and then overexpands and recompresses on the flat upper surface. These plots indicate that the smearing of shock in the inner grid has no effect on surface pressure. Additional representations of the gross characteristics of the external flow field are shown in figures 17 and 18. Figure 17 shows pressure contour plots in three planes along the vehicle. The pressures lie in a computational plane normal to the axis of the vehicle. However, when the computational plane is transformed into Cartesian space, the planes are not flat but are curved three-dimensional surfaces as they appear in this figure. Here, black represents the lowest pressure and white the highest. The extent of the bow shock is clearly visible along with the rapid expansions about the chines along the side of the vehicle. For each plane shown, the complete computational plane is not displayed, and the visual quality of the picture is therefore improved. In figure 18, Mach number contour plots are shown in planes that correspond to those used in figure 15. The Mach number contours reveal more detail of the flow in the leeward region. In the second plane, the beginning of a cross-flow shock can be seen near the upper symmetry plane near the wall. This shock can be seen quite clearly in the third or outflow plane. Also, there appears to be a small wing-body shock interaction in the third plane, as indicated by the inflection point in the bow shock near the wingtip and by the high pressure at the wingtip in the third plane of figure 17.

Figures 19 to 21 are all similar in that they show meridional distributions of nondimensional pressures along with the corresponding surface contour at three z locations along the body. The pressure is plotted as a function of y, so that the location of the pressure on the surface can be noted. The pressure is plotted on a log scale, so that pressure fluctuations on the leeward side can be seen. As expected, there is a slight rise in pressure when going from the centerline outboard at all locations. On the leeward side, pressure behaves as expected—the flow expands and compresses with corresponding changes in surface slopes. In each figure, the symbols on the surface contour plot represent the distribution of grid points on the surface.

Figure 22(a) shows an oblique view of the highly three-dimensional exit surface of the volume grid. The corresponding pressure contour plot is shown in figure 22(b).

Experimental data were taken in the Langley 31-Inch Mach 10 Tunnel at angles of attack between 15° and 30° at Reynolds numbers per foot of 0.5×10^6 and 2×10^6. The location of the moment center and the convention for positive aerodynamic coefficient are shown in figure 2. A comparison of the computed and measured axial-force coefficient C_A is shown in figure 23. For a body such as the ACRV, the predominant effect of viscous forces should appear in C_A. As shown in figure 23, the values of C_A approach the computed inviscid limit as Reynolds number is increased. However, for the normal-force coefficient C_N, shown in figure 24, there are apparently little if any viscous effects.

A comparison of the computed and measured pitching-moment coefficient C_m is presented in figure 25. The measured data indicate little if any effect of Reynolds number on C_m, and the computed, inviscid values of C_m are generally in good agreement with the measured data. The trim angle of attack inferred from both sets of data would be almost identical. There is a significant impact of Reynolds number on the lift-drag ratio, L/D, as indicated in figure 26. However, both the computed L/D and measured L/D show that, regardless of viscous effects, the maximum L/D occurs at the trim angle of attack.

Conclusions

In this paper, the tools necessary to support system studies and hypersonic aerodynamic testing of a lifting-body concept have been established. It has been demonstrated that the Langley Aerothermodynamic Upwind Relaxation Algorithm (LAURA) code, modified for inviscid computations, has the versatility and robustness to handle the flow about

complex geometries at hypersonic speeds and high angles of attack.

A methodology has been established for constructing a surface definition that meets the requirements for smoothness and continuity required for a quality computational fluid dynamics analysis. Also, a multiblock approach combined with an algebraic grid generation technique has been shown to produce a useful volume grid about a complex geometry.

The aerodynamic coefficients generated by using the grid and flow solver described herein are in very good agreement with the measured data at high Reynolds number conditions from wind-tunnel tests. Although overall vehicle characteristics, such as aerodynamic coefficients, are poor indicators of the performance of a flow solver or a grid, they do indicate that the general characteristics of the flow field are being properly modeled. A more detailed analysis of the capability of the flow solver and grid will have to await the availability of detailed surface data.

NASA Langley Research Center
Hampton, VA 23665-5225
June 24, 1991

References

1. Reinsch, Christian H.: Smoothing by Spline Functions. *Numer. Math.*, vol. 10, no. 3, 1967, pp. 177–183.

2. *Mathematical and Statistical Software at Langley.* Central Scientific Computing Complex Doc. N2-3d, NASA Langley Research Center, May 1990.

3. Smith, Robert E.; and Everton, Eric L.: Interactive Grid Generation for Fighter Aircraft Geometries. *Numerical Grid Generation in Computational Fluid Mechanics '88,* S. Sengupta, J. Häuser, P. R. Eisemann, and J. F. Thompson, eds., Pineridge Press Ltd. (United Kingdom), c.1988, pp. 805–814.

4. Smith, R. E.; and Wiese, M. R.: *Interactive Algebraic Grid-Generation Technique.* NASA TP-2533, 1986.

5. Smith, Robert E.; and Eriksson, Lars-Erik: Algebraic Grid Generation. *Comput. Methods Appl. Mech. & Eng.*, vol. 64, nos. 1–3, Oct. 1987, pp. 285–300.

6. Eriksson, L.-E.; Smith, R. E.; Wiese, M. R.; and Farr, N.: Grid Generation and Inviscid Flow Computation About a Cranked-Winged Airplane Geometry. *J. Aircr.*, vol. 25, no. 9, Sept. 1988, pp. 820–826.

7. Gnoffo, Peter A.: *An Upwind-Biased, Point-Implicit Relaxation Algorithm for Viscous, Compressible Perfect-Gas Flows.* NASA TP-2953, 1990.

8. Gnoffo, Peter A.; McCandless, Ronald S.; and Yee, H. C.: Enhancements to Program LAURA for Computation of Three-Dimensional Hypersonic Flow. AIAA-87-0280, Jan. 1987.

9. Roe, P. L.: Approximate Riemann Solvers, Parameter Vectors, and Difference Schemes. *J. Comput. Phys.*, vol. 43, no. 2, Oct. 1981, pp. 357–372.

10. Yee, H. C.: *On Symmetric and Upwind TVD Schemes.* NASA TM-86842, 1985.

11. Osher, Stanley; and Chakravarthy, Sukumar: Upwind Schemes and Boundary Conditions With Applications to Euler Equations in General Geometries. *J. Comput. Phys.*, vol. 50, no. 3, June 1983, pp. 447–481.

12. Schaefer, William T., Jr.: *Characteristics of Major Active Wind Tunnels at the Langley Research Center.* NASA TM X-1130, 1965.

13. Micol, John R.; and Weilmuenster, K. James: Experimental Aerodynamic Coefficients on a Shuttle-Like Vehicle at Mach 6 and 10 and Comparison to Prediction. AIAA-85-1796, Aug. 1985.

14. Weilmuenster, K. James; and Hamilton, H. Harris, II: A Comparison of Computed and Measured Aerodynamic Characteristics of a Proposed Aeroassist Flight Experiment Configuration. AIAA-86-1366, June 1986.

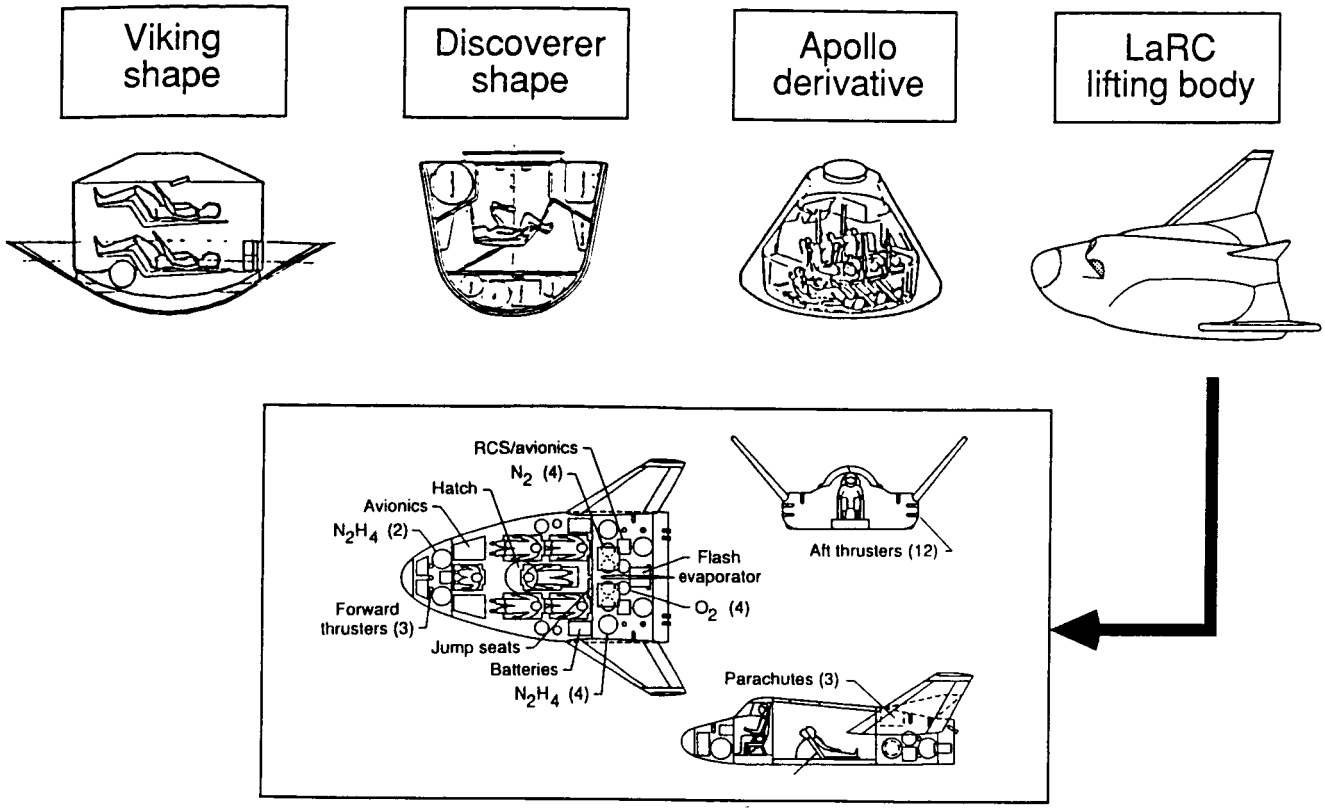

Figure 1. Proposed ACRV vehicle concepts.

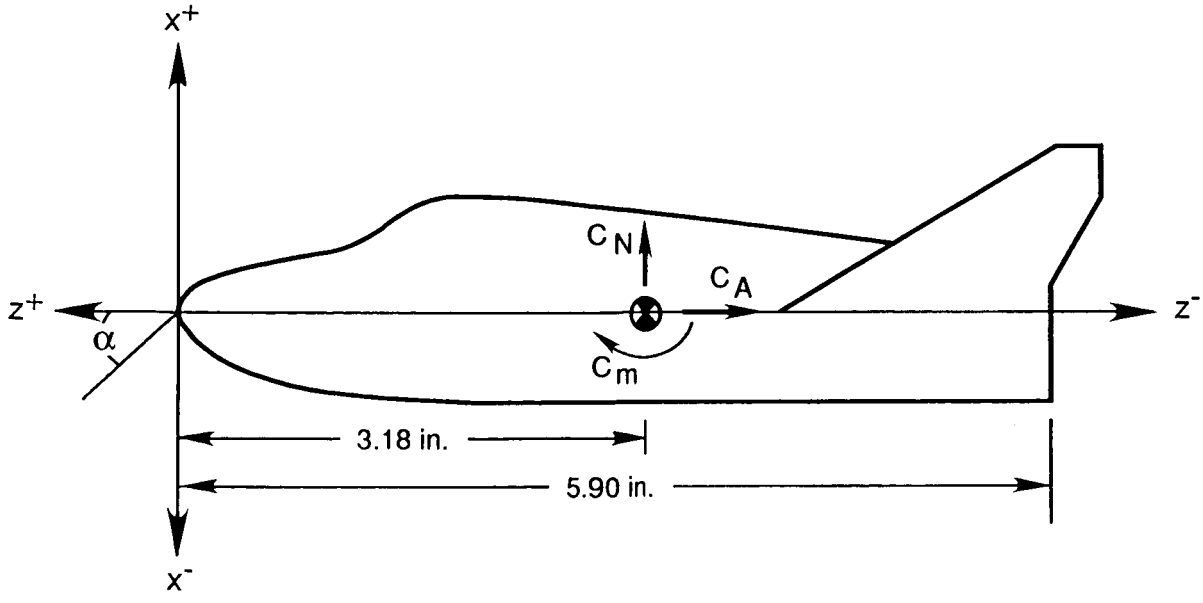

Figure 2. Coordinate system and aerodynamic coefficient convention.

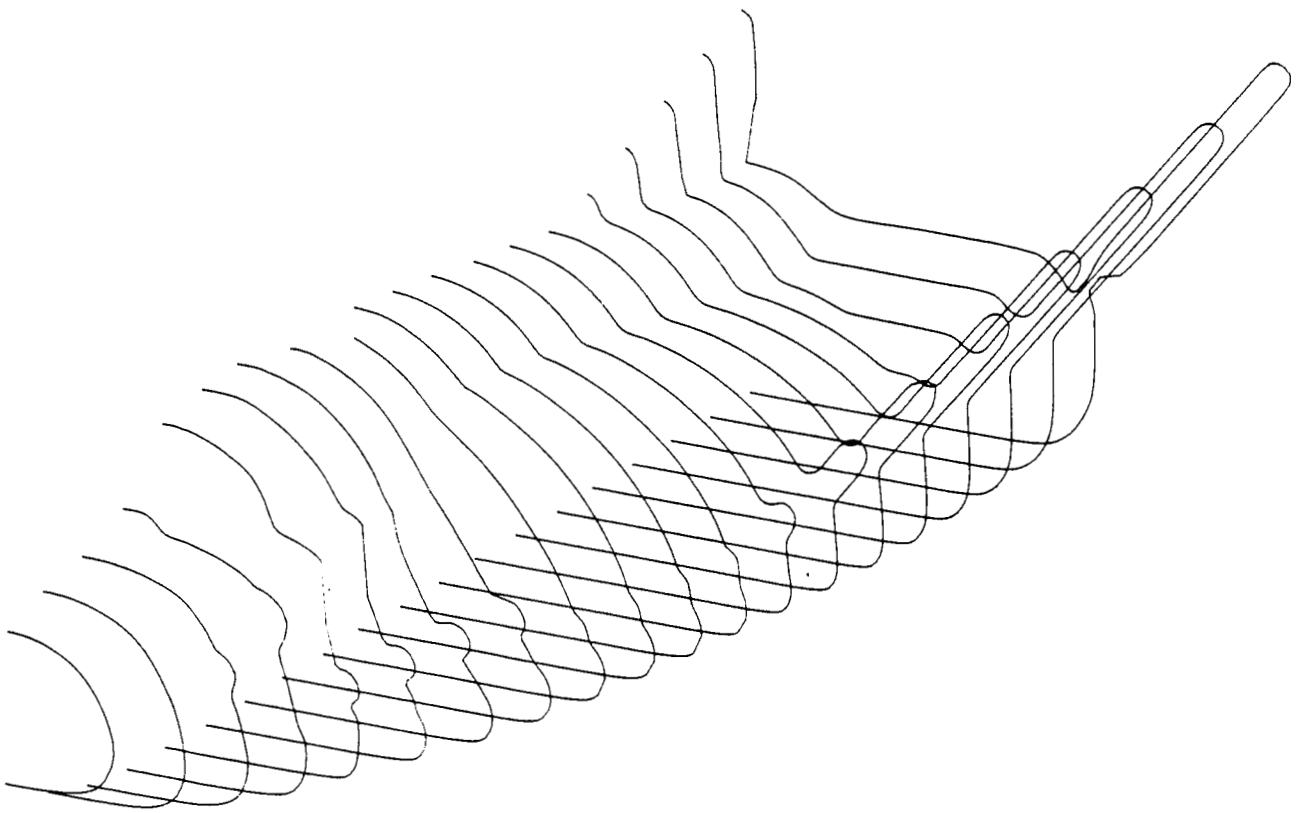

Figure 3. Original measured surface data base.

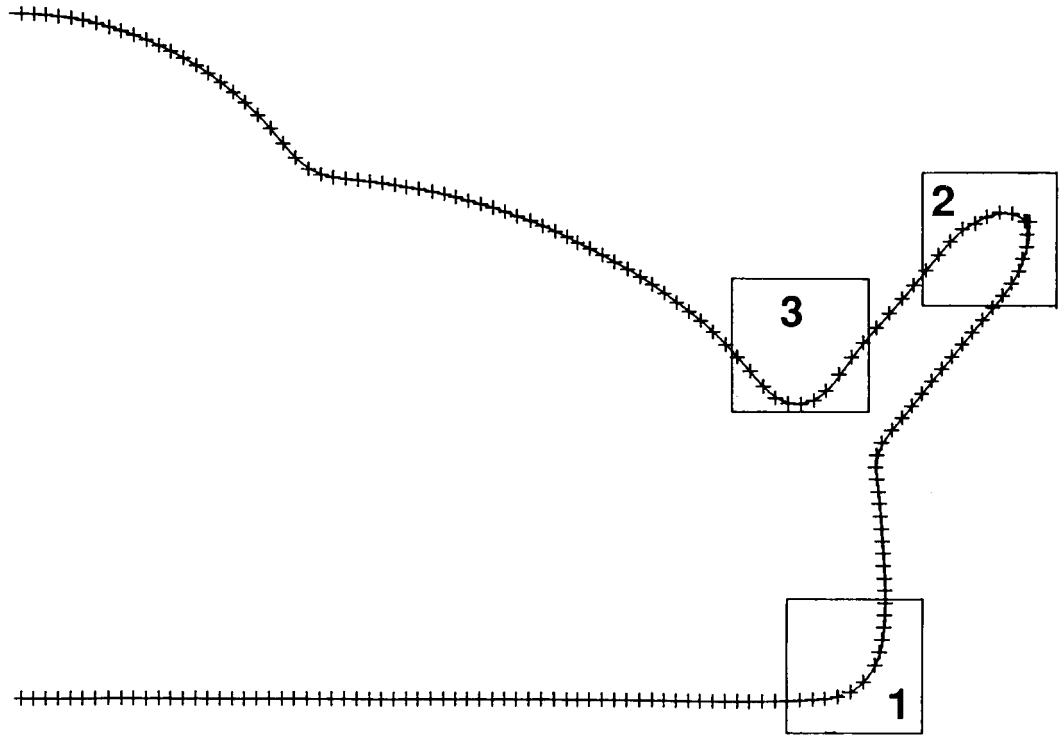

(a) Measured surface definition.

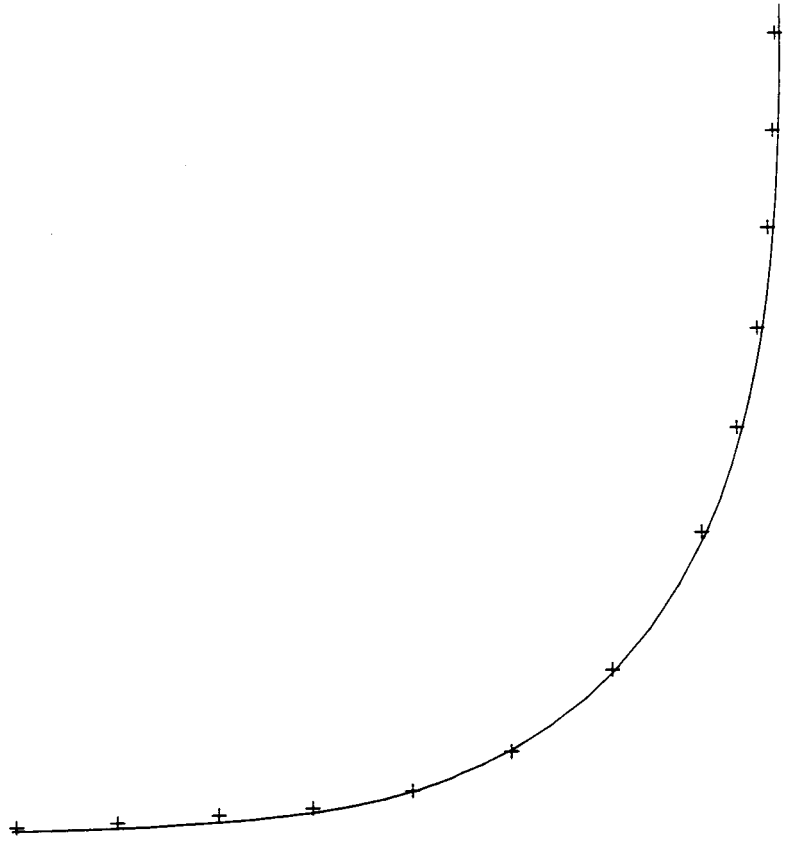

(b) Segment 1.

Figure 4. The 15th station of original measured surface points.

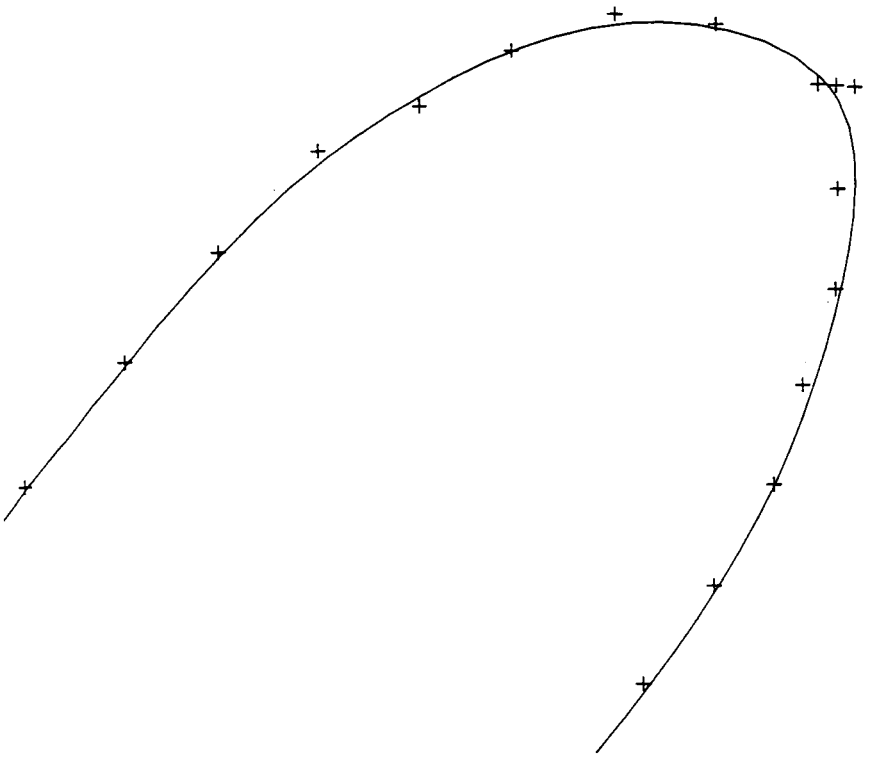

(c) Segment 2.

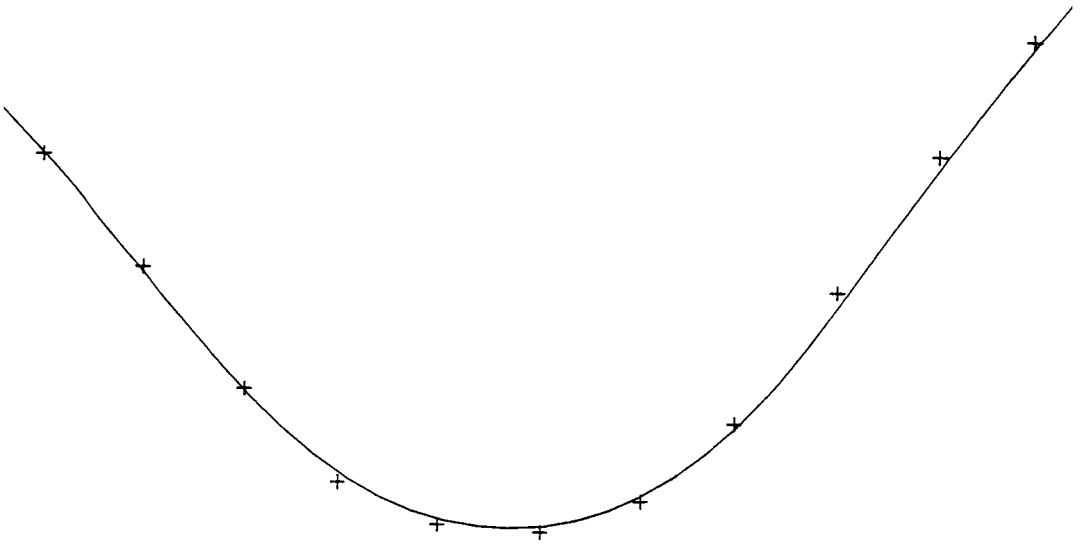

(d) Segment 3.

Figure 4. Concluded.

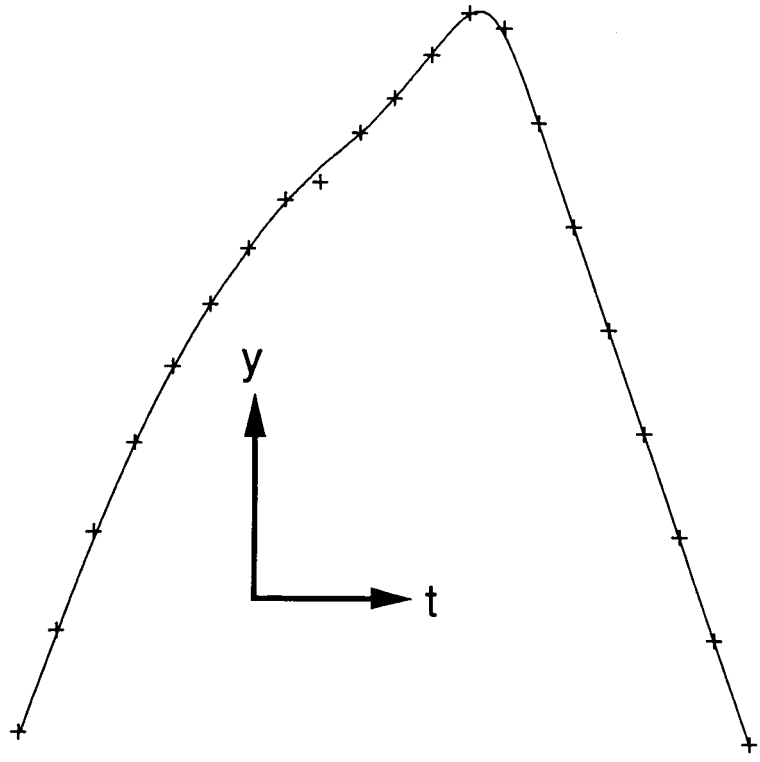

(a) y versus arc length.

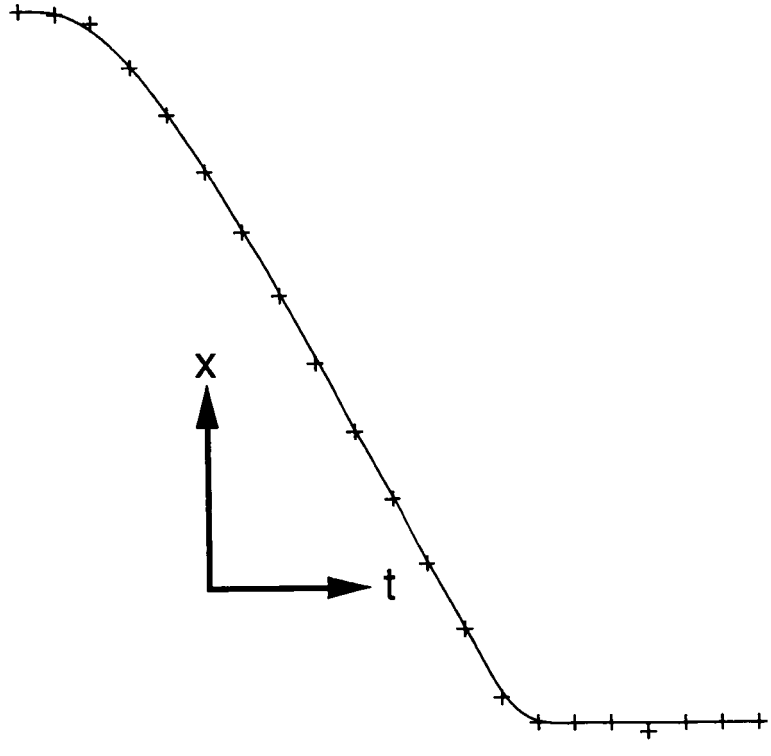

(b) x versus arc length.

Figure 5. Cross-sectional smoothing, $z = -1.845$ in.

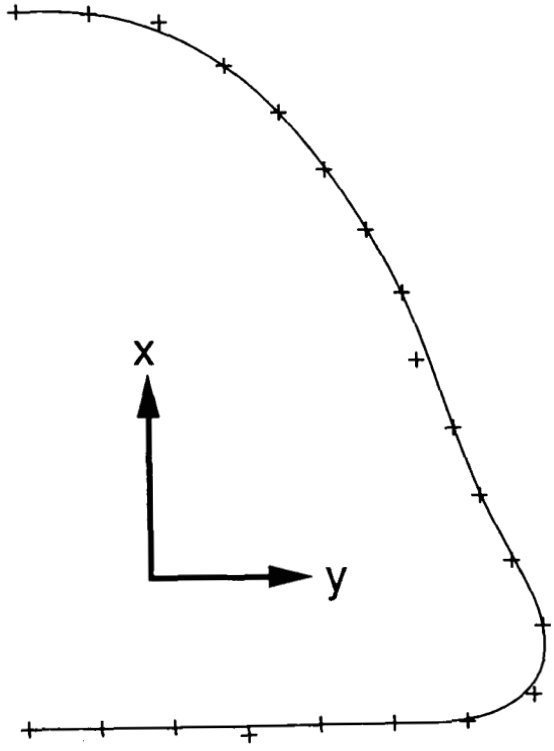

(c) Cross section.

Figure 5. Concluded.

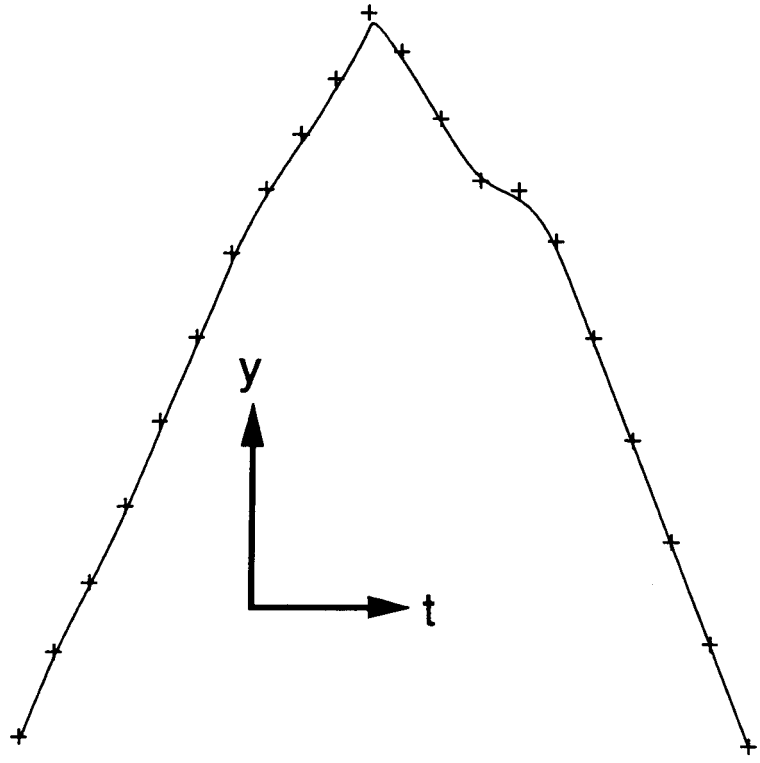

(a) y versus arc length.

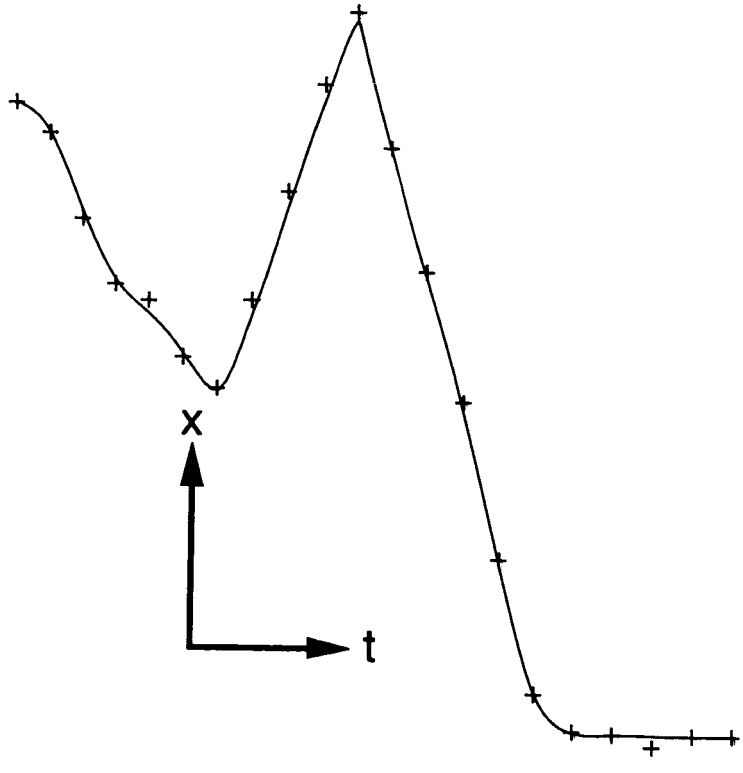

(b) x versus arc length.

Figure 6. Cross-sectional smoothing, $z = -5.051$ in.

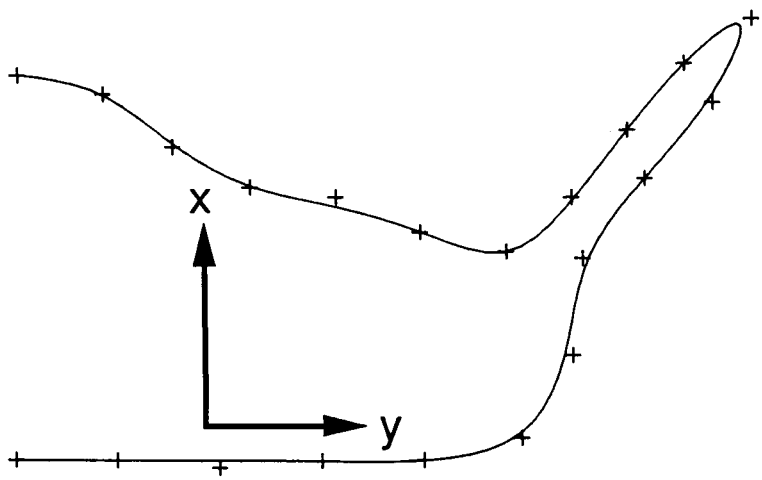

(c) Cross section.

Figure 6. Concluded.

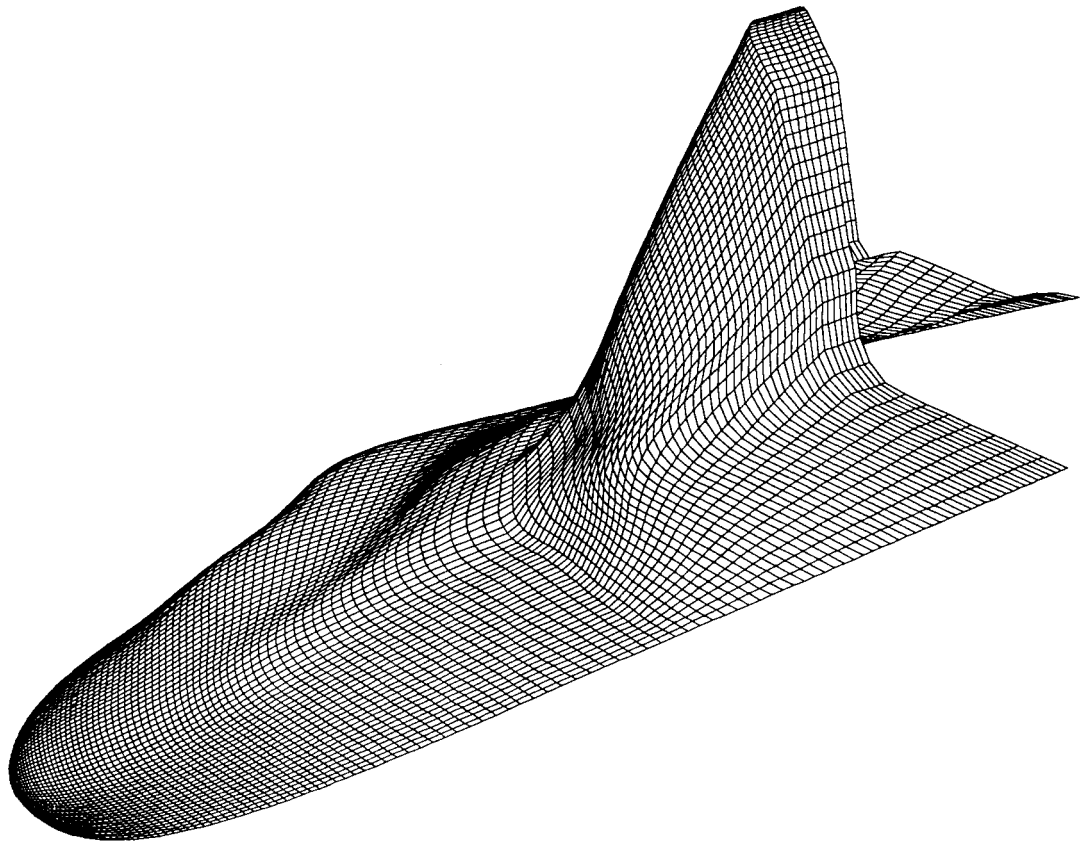

Figure 7. ACRV vehicle surface grid.

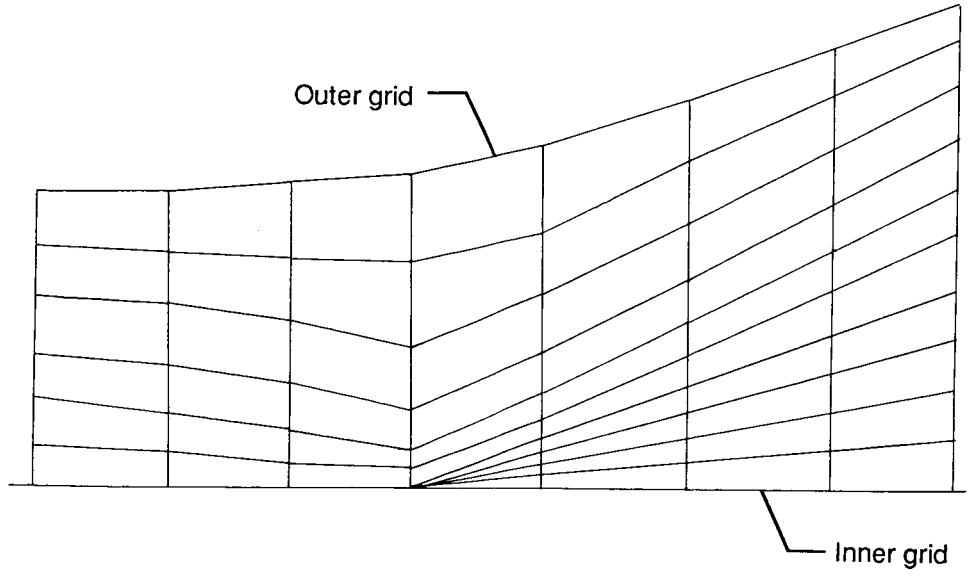

Figure 8. Two-block grid topology.

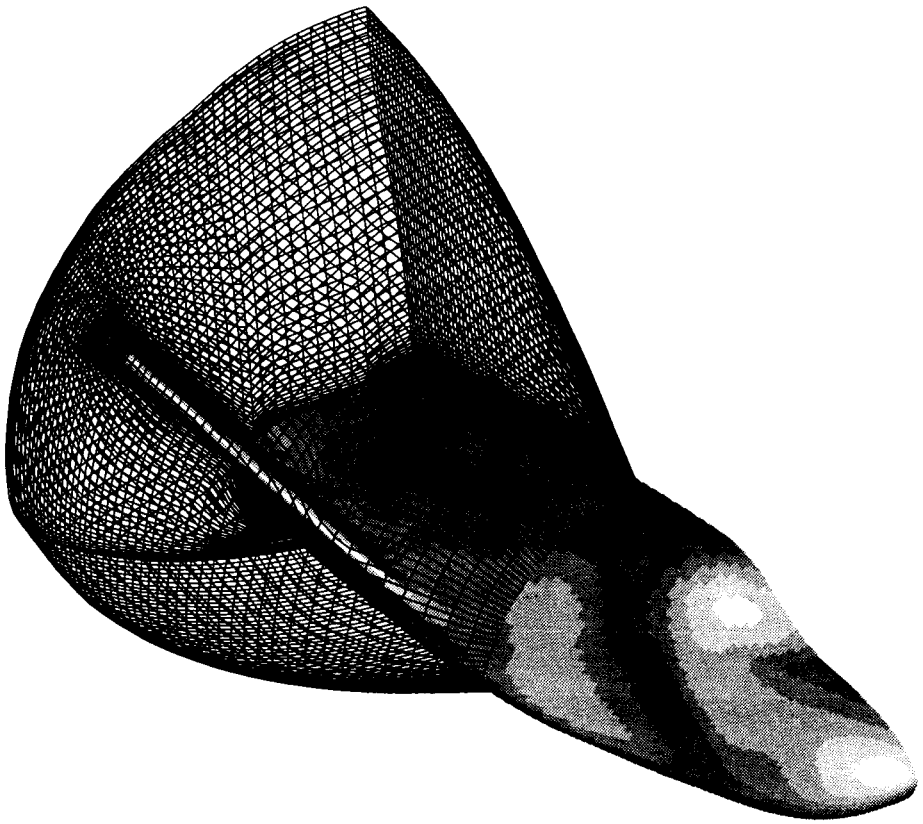

Figure 9. Boundaries of inner grid.

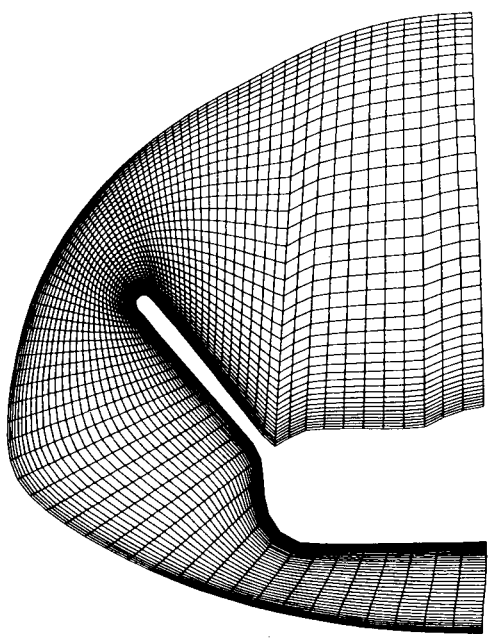

Figure 10. Inner grid on downstream boundary surface.

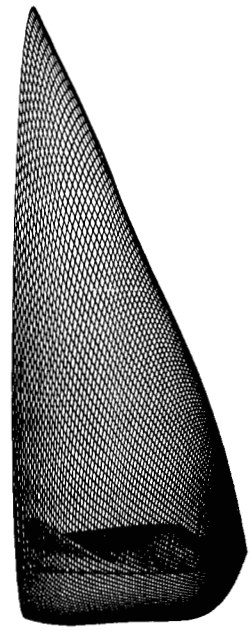

Figure 11. Far-field boundary surface.

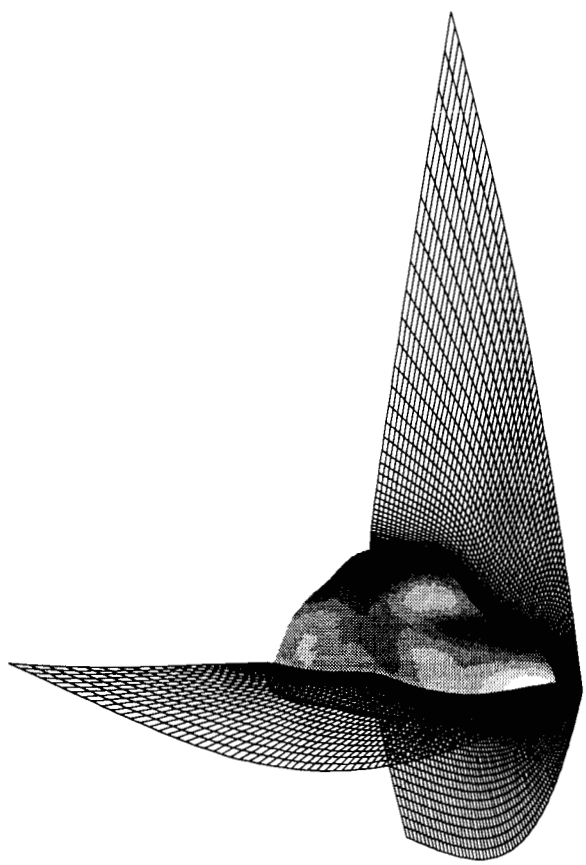

Figure 12. Forward outer-block construction.

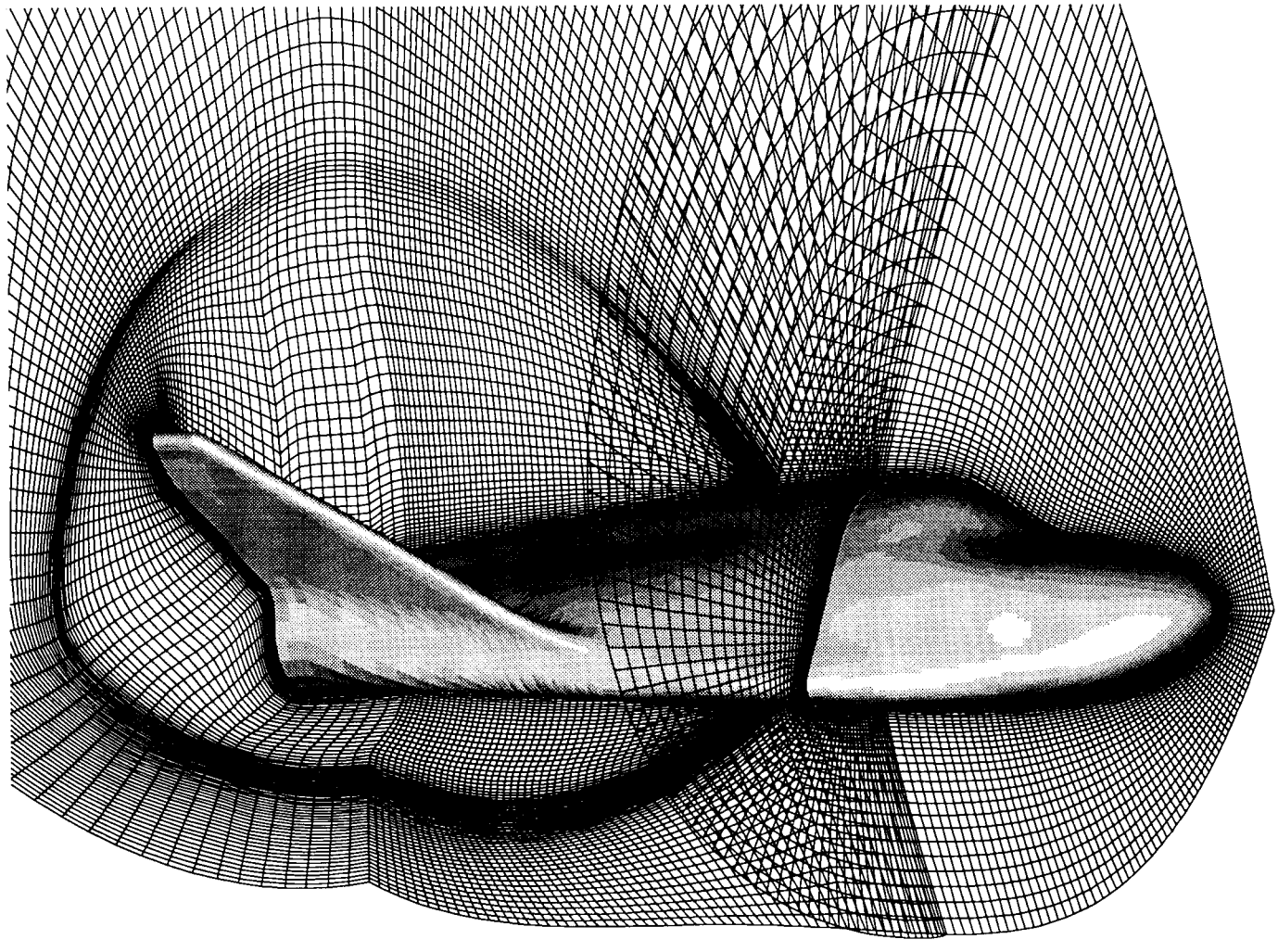

Figure 13. Composite of grids in symmetry plane and two spanwise surfaces.

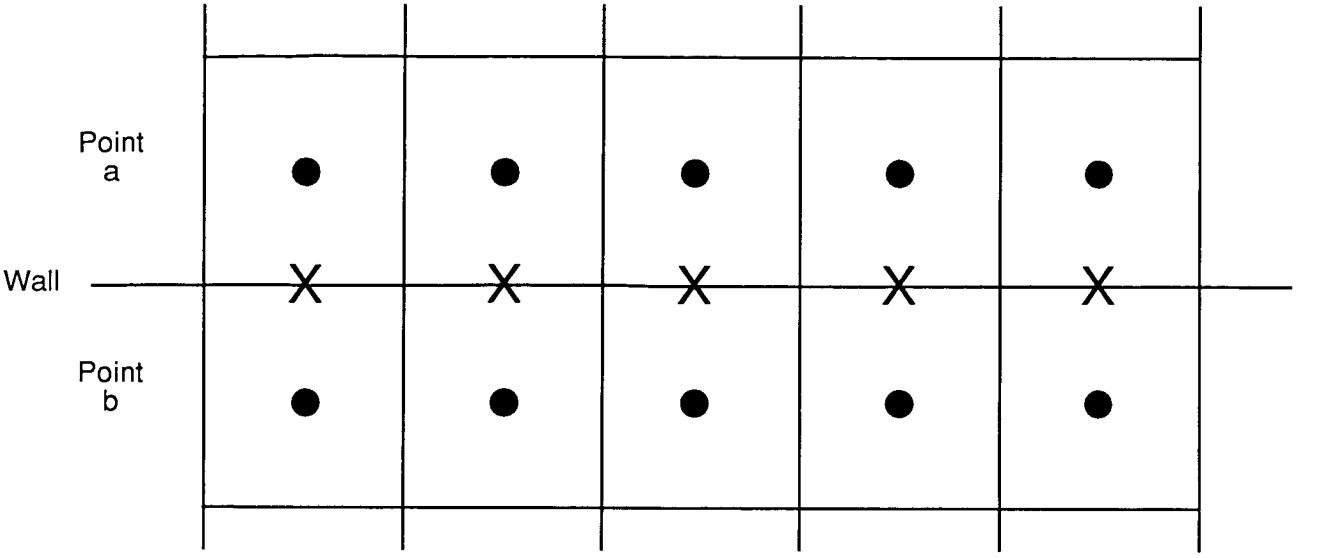

Figure 14. Schematic of wall boundary treatment.

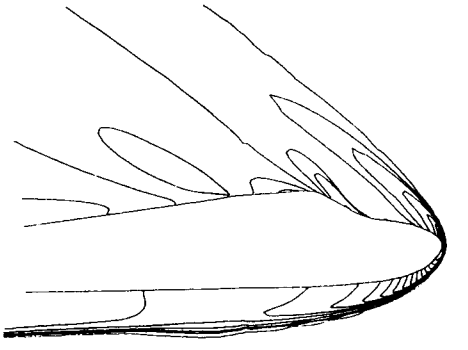

Figure 15. Symmetry-plane pressure contours. $M_\infty = 10$; $\alpha = 25°$.

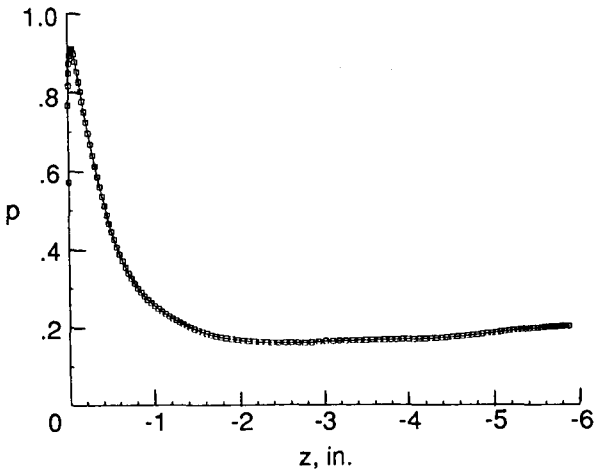

(a) Windward surface.

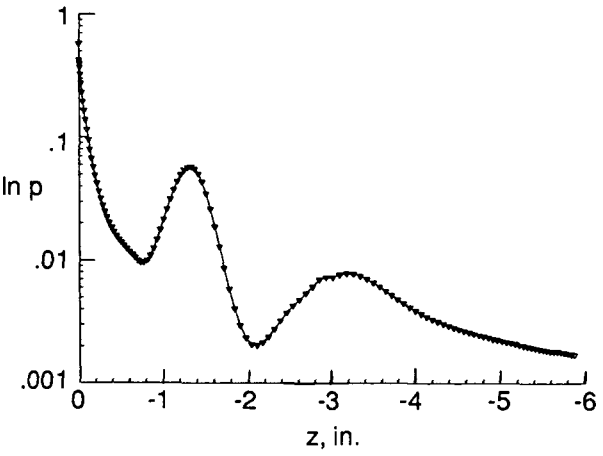

(b) Leeward surface.

Figure 16. Surface pressure in symmetry plane. $M_\infty = 10$; $\alpha = 25°$; $\gamma = 1.4$.

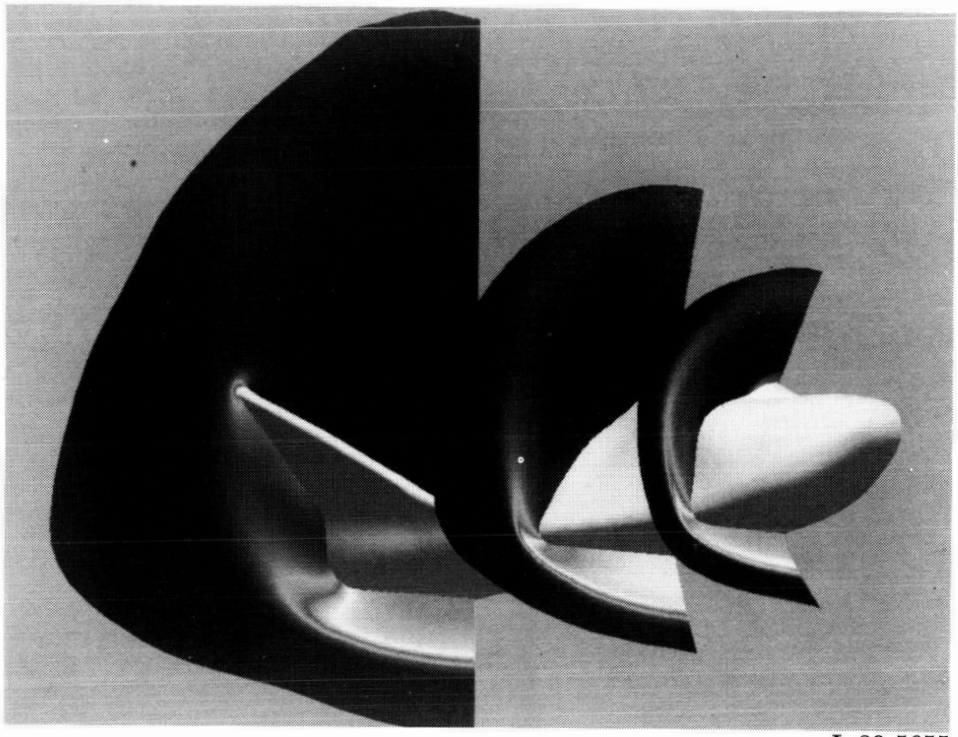

L-89-5655

Figure 17. Pressure contour plots. $M_\infty = 10;\ \alpha = 25°; \gamma = 1.4$.

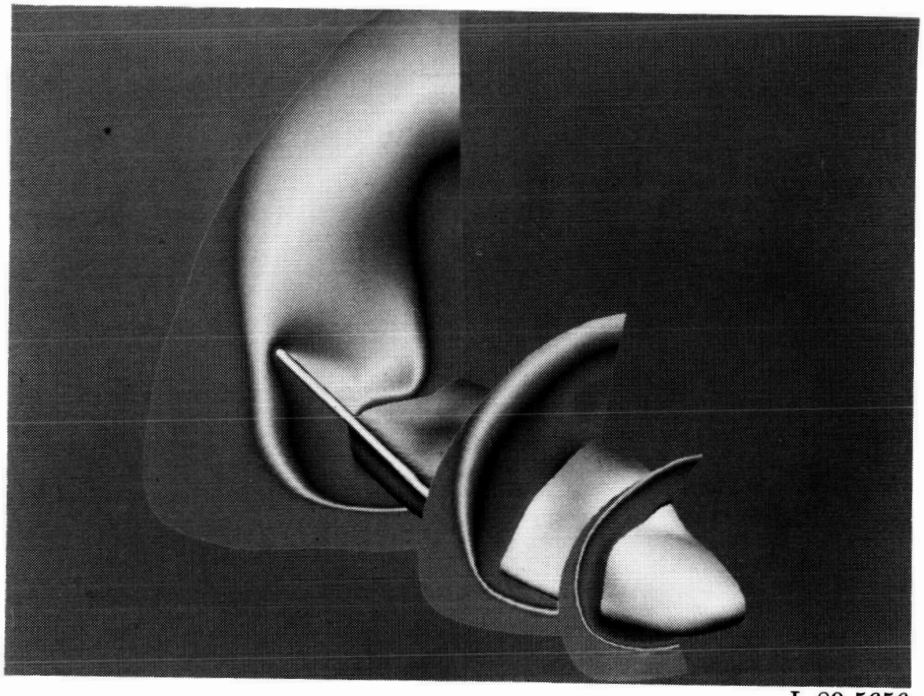

L-89-5656

Figure 18. Mach number plots. $M_\infty = 10;\ \alpha = 25°; \gamma = 1.4$.

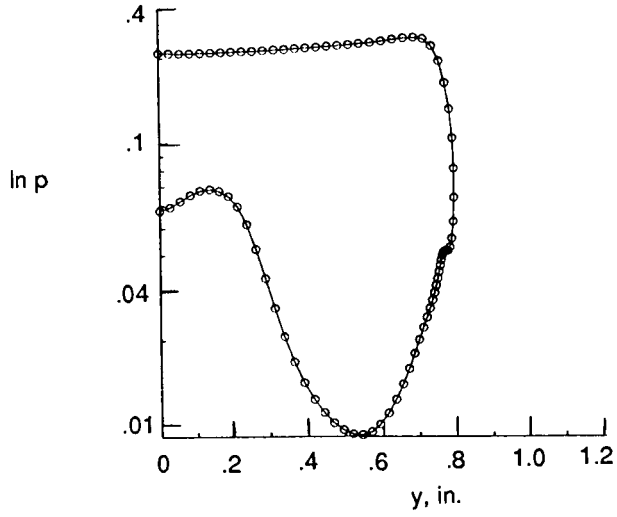

(a) Pressure.

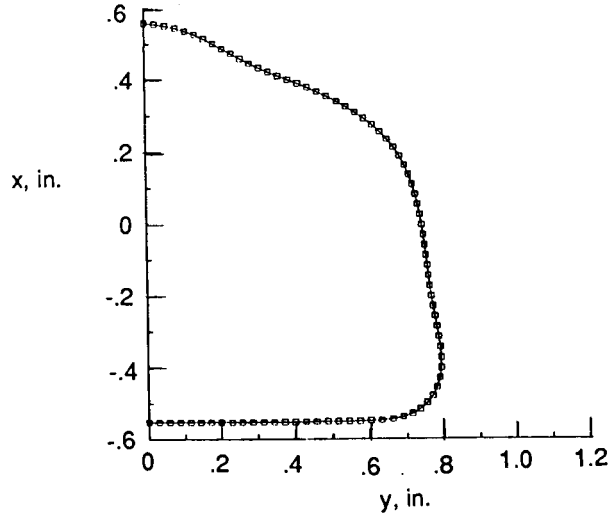

(b) Surface contour.

Figure 19. Pressure and surface contours at $z = -1.34$ in. $M_\infty = 10$; $\alpha = 25°$; $\gamma = 1.4$.

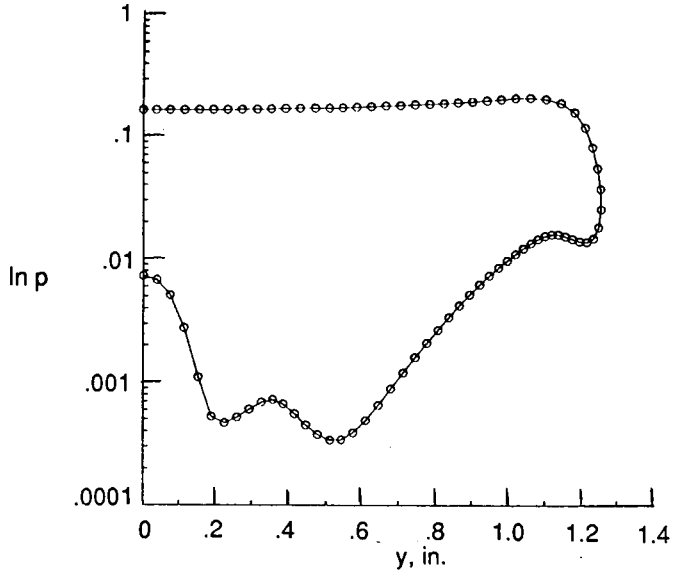

(a) Pressure.

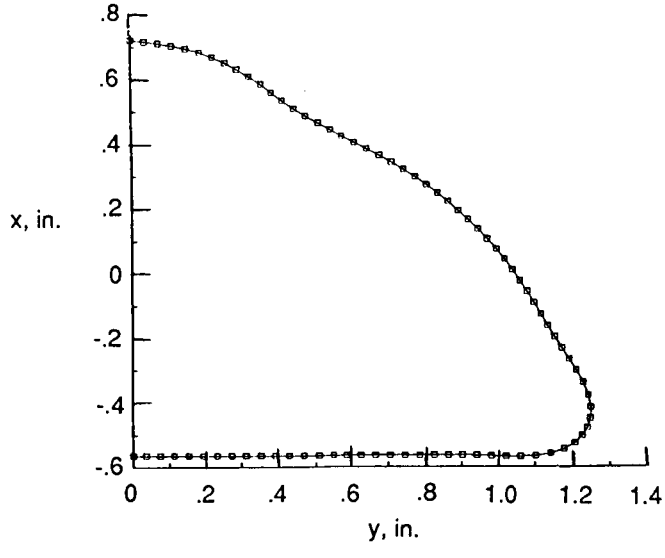

(b) Surface contour.

Figure 20. Pressure and surface contours at $z = 2.69$ in. $M_\infty = 10$; $\alpha = 25°$; $\gamma = 1.4$.

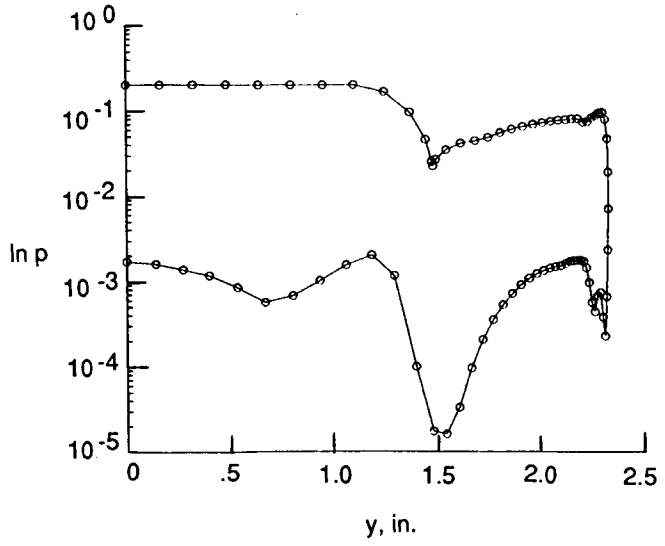

(a) Pressure.

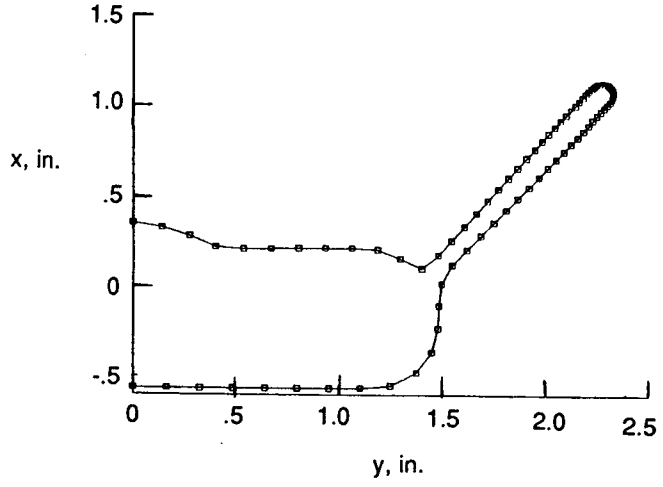

(b) Surface contour.

Figure 21. Pressure and surface contours at exit plane. $M_\infty = 10$; $\alpha = 25°$; $\gamma = 1.4$.

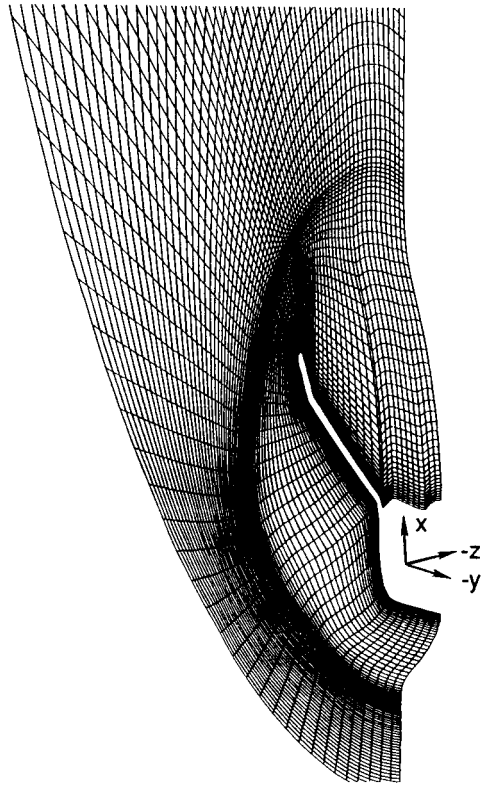

(a) Grid.

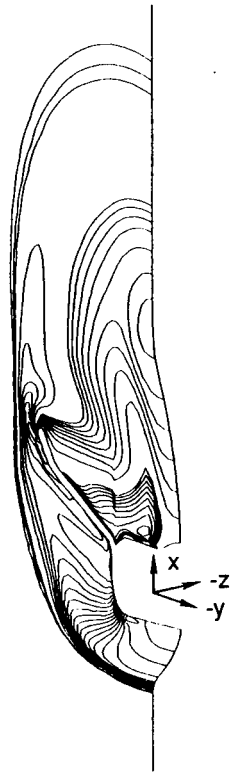

(b) Pressure contours.

Figure 22. Grid and pressure contour plots in exit plane.

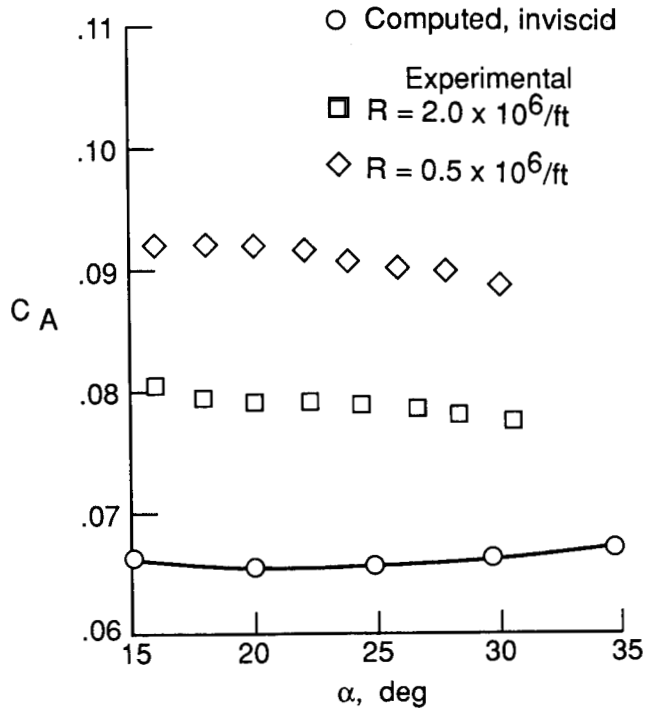

Figure 23. Computed and measured axial-force coefficients. $M_\infty = 10$ and $\gamma = 1.4$.

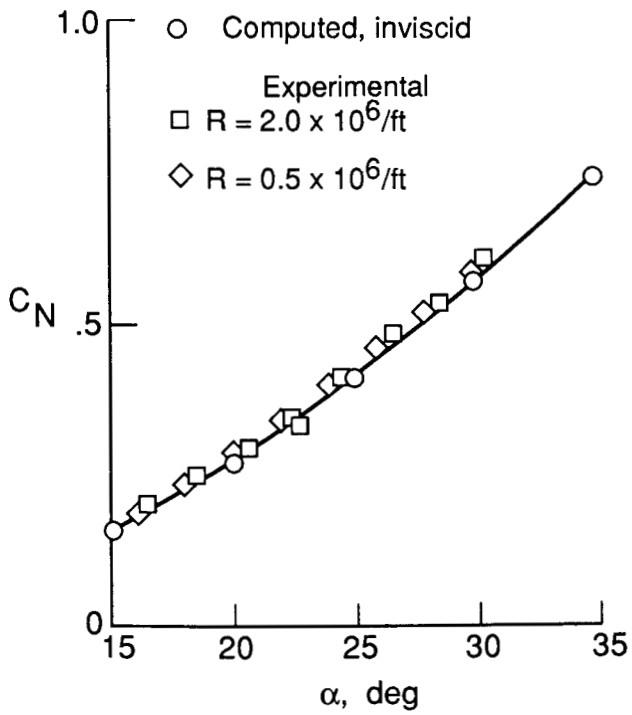

Figure 24. Computed and measured normal-force coefficients. $M_\infty = 10$ and $\gamma = 1.4$.

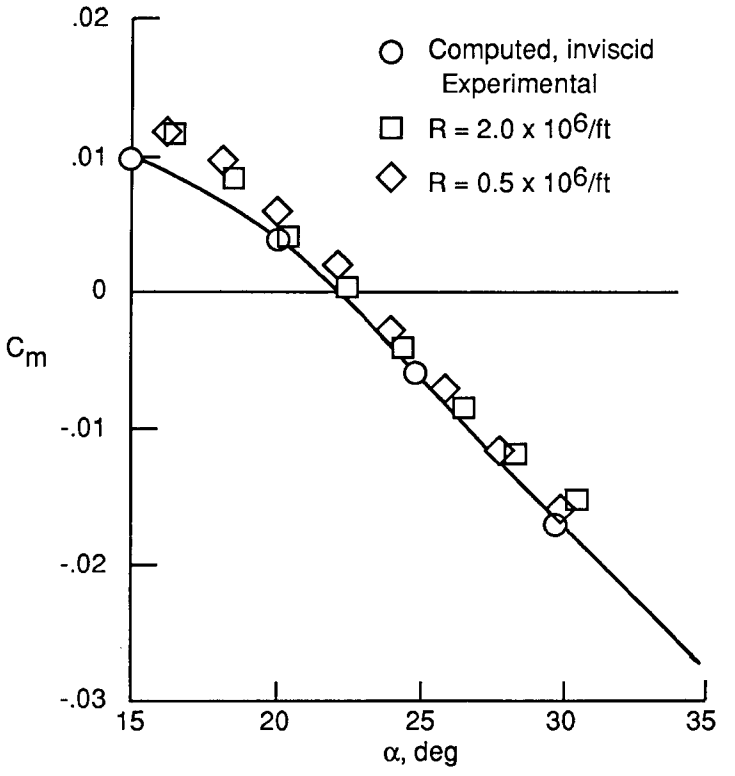

Figure 25. Comparison of computed and measured pitching-moment coefficients.

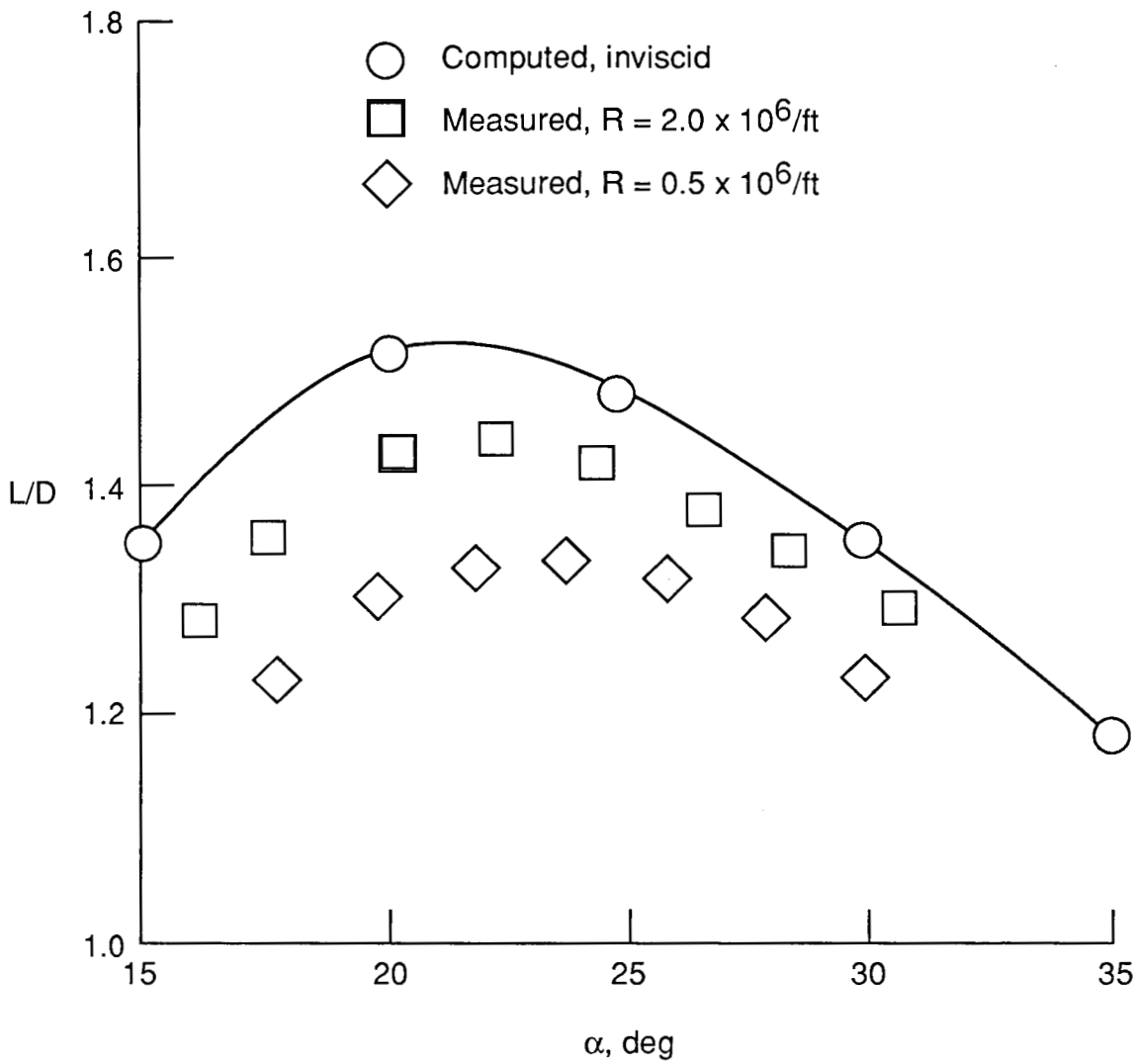

Figure 26. Comparison of computed and measured lift-drag ratios.

NASA
National Aeronautics and Space Administration

Report Documentation Page

1. Report No.	2. Government Accession No.	3. Recipient's Catalog No.
NASA TP-3101		

4. Title and Subtitle	5. Report Date
Numerical Analysis and Simulation of an Assured Crew Return Vehicle Flow Field	September 1991
	6. Performing Organization Code

7. Author(s)	8. Performing Organization Report No.
K. James Weilmuenster, Robert E. Smith, Jr., and Francis A. Greene	L-16836

9. Performing Organization Name and Address	10. Work Unit No.
NASA Langley Research Center Hampton, VA 23665-5225	506-40-91-01
	11. Contract or Grant No.

12. Sponsoring Agency Name and Address	13. Type of Report and Period Covered
National Aeronautics and Space Administration Washington, DC 20546-0001	Technical Paper
	14. Sponsoring Agency Code

15. Supplementary Notes

16. Abstract

A lifting body has been proposed as a candidate for the ACRV (assured crew return vehicle), which will serve as the crew rescue vehicle for Space Station *Freedom*. The focus of this work is on body surface definition, surface and volume grid definition, and the computation of inviscid flow fields about the vehicle at wind-tunnel conditions. Very good agreement is shown between the computed aerodynamic characteristics of the vehicle at Mach 10 and those measured in wind-tunnel tests at high Reynolds numbers.

17. Key Words (Suggested by Author(s))	18. Distribution Statement
Grid generation Computational fluid dynamics Hypersonic flow Lifting-body entry vehicle	Unclassified—Unlimited Subject Category 34

19. Security Classif. (of this report)	20. Security Classif. (of this page)	21. No. of Pages	22. Price
Unclassified	Unclassified	35	A03

For sale by the National Technical Information Service, Springfield, Virginia 22161-2171